

1 **Detrital garnet geochronology by in-situ U-Pb and Lu-Hf analysis: A case study**
2 **from the European Alps**

3
4 **Chris Mark^{1*}, Gary O'Sullivan¹, Stijn Glorie², Alexander Simpson², Sergio Andò³,**
5 **Marta Barbarano³, Laura Stutenbecker⁴, and J. Stephen Daly^{1,5}**

6 ¹UCD School of Earth Sciences and UCD Earth Institute, University College Dublin,
7 Belfield, Dublin 4, Ireland.

8 ²Department of Earth Sciences, University of Adelaide, Adelaide, Australia.

9 ³Department of Earth and Environmental Sciences, Università di Milano-Bicocca, Milan,
10 Italy.

11 ⁴Institute of Geology and Paleontology, Westfälische Wilhelms-Universität Münster,
12 Münster, Germany.

13 ⁵Science Foundation Ireland Research Centre in Applied Geosciences (iCRAG), University
14 College Dublin, Belfield, Dublin 4, Ireland.

15 Corresponding author: Chris Mark (chris.mark@nrm.se)

16 *Now at: Department of Geosciences, Swedish Museum of Natural History, Stockholm,
17 Sweden.

18 **Key Points:**

- 19 • Detrital garnet U-Pb and Lu-Hf ages preferentially record the most recent
20 metamorphic event in the source area;
- 21 • Both systems are less refractory than alternative detrital U-Pb geochronometers;
- 22 • Age recovery for Lu-Hf in garnet is considerably better than for U-Pb.
- 23

24 Abstract

25 Detrital geochronology employing the widely-used zircon U-Pb proxy is biased towards
 26 igneous events and metamorphic anataxis; additionally, zircon is highly refractory and
 27 frequently polycyclic. Garnet, a rock-forming and thus commonly-occurring mineral, is
 28 predominantly metamorphic and much less refractory. Here, we report in-situ U-Pb and Lu-Hf
 29 ages from detrital garnet hosted in ancient and modern sediments of the European Alps. Both
 30 geochronometers are biased towards the most recent garnet-crystallising metamorphic event in
 31 the source area, with fewer inherited ages. This likely reflects efficient removal of inherited
 32 garnet during diagenesis and metamorphism, and is in contrast to detrital zircon, apatite, and
 33 rutile U-Pb data which largely record pre-Alpine ages. Neither the U-Pb nor Lu-Hf system in
 34 garnet exhibits a relationship between age recovery and composition. However, the Lu-Hf
 35 system in garnet yields significantly better age recovery than the U-Pb system. Estimated initial
 36 $^{238}\text{U}/^{206}\text{Pb}_c$ values at the time of crystallization are near unity for the garnet analysed in this
 37 study, suggesting that garnet does not significantly partition U from Pb during crystallization,
 38 at least for the generally almandine-rich garnets analysed in this study. Hence, Lu-Hf
 39 geochronology of detrital garnet offers an effective method to detect and date the most recent
 40 phase of mid-grade metamorphism in sub-anatectic source areas, in which detrital zircon U-Pb
 41 analysis may be of less utility.

42 Plain Language Summary

43 Mountain ranges are characterized by rapid changes in their constituent rocks as these undergo
 44 metamorphism to adjust to increasing pressure and temperature during burial. These
 45 metamorphic processes drive mineral crystallization. Once cooled, each mineral acts as a
 46 geochemical reservoir isolated from the surrounding environment. Therefore, if a mineral has
 47 incorporated a radioactive isotope during crystallization, it can be dated to constrain the timings
 48 and rates of metamorphism. As erosion ultimately converts crystalline bedrock to sediment,
 49 the geological histories of these processes are preserved in the sediment shed during erosion.
 50 Consequently, these histories can be read from sedimentary rocks in adjacent sedimentary
 51 basins. Minerals traditionally used to study the sources of these sediments, such as zircons,
 52 largely grow from molten rock rather than during metamorphism, and are tough enough to be
 53 recycled through multiple tectonic events. The mineral garnet more commonly grows under
 54 metamorphic conditions and is more thus more effective at directly recording the most recent
 55 phases of significant mountain building. Here, we present uranium-lead and lutetium-hafnium
 56 ages of garnet in modern and ancient sediment from the Alps. We show that garnet
 57 preferentially records Alpine events, and is thus suitable for provenance studies targeting the
 58 most recent mountain building event.

59 1 Introduction

60 1.1 The utility of detrital garnet in sedimentary provenance analysis

61 Detrital geochronology is a powerful tool for interrogating the sedimentary archive of
 62 paleo-hinterland tectonic, metamorphic, and climatic processes, and can also be applied to
 63 modern river sediment as a first-pass tool to establish regional bedrock ages (e.g., von Eynatten
 64 & Dunkl, 2012; Ledent et al., 1964; Machado & Gauthier, 1996; Najman, 2006). The zircon
 65 U-Pb detrital geochronometer has seen widespread adoption in provenance analysis (3,626 of
 66 4,471 results for the search term *detrital geochronology* also contain the term *zircon U-Pb*;
 67 Clarivate Analytics Web of Science). However, zircon fertility is strongly biased towards
 68 intermediate to felsic source rocks (Boehnke et al., 2013). Moreover, zircon neocrystallization
 69 is volumetrically limited in metamorphic terranes which do not achieve anatexis (e.g., Moecher
 70 & Samson, 2006), and is typically restricted to rim overgrowths which are vulnerable to

71 mechanical destruction during fluvial transport, and which are also challenging to detect and
 72 analyse (e.g., Campbell et al., 2005).

73 Therefore, it is desirable to develop complementary provenance tools to identify
 74 metamorphic source rocks in the detrital record (Zack et al., 2011). Garnet group minerals are
 75 rock-forming in several common metamorphic lithologies and are also present as accessory
 76 minerals in a wide range of igneous and metamorphic rocks. Garnet is therefore a common
 77 constituent of clastic detritus from orogens. Here and throughout, we use the term *garnet* as a
 78 synonym for garnet group silicates in the garnet supergroup. These have the general formula
 79 $X_3Y_2Z_3O_{12}$ in which the Z-site is occupied by Si; the fourteen known end members of this
 80 complex solid solution include the geologically common varieties almandine $Fe_3Al_2(SiO_4)_3$,
 81 andradite $Ca_3Fe_2(SiO_4)_3$, grossular $Ca_3Al_2(SiO_4)_3$, spessartine $Mn_3Al_2(SiO_4)_3$, pyrope
 82 $Mg_3Al_2(SiO_4)_3$, and uvarovite $Ca_3Cr_2(SiO_4)_3$ (Grew et al., 2013).

83 The wide range of documented stoichiometry, and potential for correlation to source
 84 rock type, has resulted in extensive use of garnet composition as a detrital provenance tool
 85 (Connally, 1964; Morton, 1985; Schönig et al., 2021; Stutenbecker et al., 2017; Suggate &
 86 Hall, 2014). Importantly, the broad P-T stability range of garnet in most bulk rock compositions
 87 means that neocrystalline garnet is shed to the sediment routing network during almost every
 88 orogenic exhumational phase, beginning with epidote-garnet dominated heavy mineral
 89 assemblages from upper-greenschist-facies-grade metasedimentary cover units, through
 90 gneissose hornblende-garnet-epidote-aluminosilicate suites, culminating in debris from garnet-
 91 cordierite bearing leucogranites generated by anataxis (Andò et al., 2013; Garzanti et al.,
 92 2010a). Garnet group minerals comprise 5-42 % of the heavy mineral fraction in the bedload
 93 of rivers draining major modern orogens where sediment production is dominated by rapid
 94 exhumation of metamorphic crystalline bedrock, including the Po, Ganges-Brahmaputra, and
 95 Indus (Garzanti et al., 2005; Garzanti and Andò, 2007; Garzanti et al., 2010a; Garzanti et al.,
 96 2010b). In rivers draining tectonically quiescent continental interiors characterized by
 97 widespread ancient sedimentary cover, the garnet fraction is typically < 7 %, including the
 98 Amazon, Congo, Mississippi, Nile, and Zambezi (Garzanti et al., 2015, 2019, 2021; Mange &
 99 Otvos, 2005; do Nascimento et al., 2015).

100 Despite the abundance of garnet in recent surficial sediments, it is only moderately
 101 stable during burial and diagenesis. Studies of Cenozoic-Mesozoic depocenters in the North
 102 Sea, Nile Delta, Bay of Bengal and Gulf of Mexico indicate that near-complete dissolution of
 103 sand-grade garnet occurs at burial depths of 4-5 km (Andò et al., 2012; Garzanti et al., 2018;
 104 Milliken, 2007; Morton & Hallsworth, 2007). Garnet is also rapidly destroyed by prolonged
 105 residence in soils (Velbel, 1984; Andò et al., 2012). As a result, garnet is considerably less
 106 refractory than other commonly-used detrital U-Pb geochronometers including zircon, rutile,
 107 apatite, but more so than titanite, which is typically removed at 3-4 km burial depths (Andò et
 108 al., 2012; Garzanti et al., 2018; Morton & Hallsworth, 2007). Recycling of detrital garnet into
 109 younger orogens is thus expected to be rare, although it has been reported (Manzotti &
 110 Ballèvre, 2013). Garnet is also commonly eliminated from metasediment during the early
 111 stages of metamorphism (Cave et al., 2015), but preservation of inherited garnet retained in
 112 polycyclic crystalline bedrock has also been reported (Walker et al., 2021; Argles et al., 1999).
 113 Significantly, a compositional control on garnet diagenetic stability has been documented, with
 114 a decrease in the Ca content of bulk garnet separates with burial depth and an increase in Fe
 115 content (Morton & Hallsworth, 2007). As Mn and Mg contents in that example remained
 116 unchanged, this could indicate higher diagenetic vulnerability of grossular- and uvarovite-rich
 117 garnets.

118

119 1.2 Garnet geochronology

120 In crystalline bedrock, garnet is datable using the Rb-Sr, Sm-Nd, Lu-Hf, and U-Pb
 121 radioisotope systems. As with many geochronometers, the garnet host seldom completely
 122 excludes the daughter element during crystal growth: the isotopic composition of the initial
 123 daughter component must therefore be corrected during age calculation, normally by the
 124 isochron method (Nicolaysen, 1961). Garnet typically has very low Rb/Sr ratios, so the
 125 $^{87}\text{Rb}/^{86}\text{Sr}$ age is normally calculated as a model age from $^{87}\text{Sr}/^{86}\text{Sr}$, requiring assumptions
 126 regarding matrix Rb/Sr during garnet growth which cannot easily be verified in a detrital
 127 context (Christensen et al., 1989). Typical $^{147}\text{Sm}/^{144}\text{Nd}$ ratios, while higher than $^{87}\text{Rb}/^{86}\text{Sr}$, are
 128 also low (typically < 3 except in highly fractionated rocks such as pegmatites; Thöni, 2003).
 129 Coupled with the long half-life of ^{147}Sm , analysis of a co-crystallising phase with lower initial
 130 Sm/Nd is required to anchor the Sm-Nd isochrons (e.g., Baxter & Scherer, 2013). Low Sm/Nd
 131 and slow radiogenic ingrowth probably renders impractical the use of detrital single-garnet Sm-
 132 Nd analyses coupled with initial $^{143}\text{Nd}/^{144}\text{Nd}$ estimates obtained from Nd isotope terrestrial
 133 evolution models (e.g., DePaolo & Wasserburg, 1976). This hinders application of the Sm-Nd
 134 technique to detrital studies. Although co-analysis of either bulk sediment hosting the detrital
 135 grains (Oliver et al., 2000) or garnet-hosted inclusions have been employed to allow
 136 construction of single-grain isochrons (Maneiro et al., 2019), both methods are somewhat
 137 laborious.

138 In contrast, the half-lives of ^{176}Lu and $^{238,235}\text{U}$ are shorter than for ^{87}Rb and ^{147}Sm ,
 139 leading to faster radiogenic ingrowth. More importantly, initial $^{176}\text{Lu}/^{176}\text{Hf}$ in garnet is typically
 140 high (Duchêne et al., 1997) and the terrestrial range of initial Hf isotopic compositions is small
 141 (e.g., Vervoort et al., 1999), such that correction for initial Hf becomes relatively trivial at the
 142 level of precision typically required for detrital studies (Simpson et al., 2021). Empirical and
 143 experimental studies show that the initial U/Pb ratio in garnet can be high (Haack & Gramse,
 144 1972; Hauri et al., 1994); moreover, the relatively predictable isotopic evolution of crustal Pb
 145 (Stacey & Kramers, 1975) facilitates correction of single-analysis U-Pb ages for initial Pb using
 146 the same approach typically employed for detrital analysis of other common-Pb hosting phases
 147 (e.g., Chew et al., 2020). Both techniques are therefore suitable in principle for detrital single-
 148 grain analysis.

149 Lu-Hf dating of garnet, initially by solution and now by *in-situ* methods, is
 150 uncontroversial (Duchêne et al., 1997; Simpson et al., 2021). In contrast U-Pb dating of garnet,
 151 despite having a longer history (Burton et al., 1995; Mezger et al., 1989), has been the subject
 152 of debate centered around whether U is hosted in the garnet lattice, or as inclusions which may
 153 be inherited (DeWolf et al., 1996). However, multiple lines of evidence support incorporation
 154 of U in garnet as a trace element, although the mechanisms of incorporation and extent of
 155 possible stoichiometric controls remain unclear. Dissolution of bulk detrital garnet separates
 156 obtained from modern bedload of the Brahmaputra river indicated an average U content of 3.5
 157 $\mu\text{g/g}$, although co-dissolution of U-hosting inclusions cannot be excluded (Garçon et al., 2014).
 158 In-situ empirical studies by etching of spontaneous fission tracks or ion microprobe analysis
 159 have demonstrated homogeneously-distributed U in garnet up to several hundred $\mu\text{g/g}$ (Haack
 160 & Gramse, 1972; Smith et al., 2004), with andradite and spessartine typically containing higher
 161 U concentrations than almandine, pyrope, or grossular. Experimental synthesis of pyrope-rich
 162 and pyrope-grossular garnet from silicate melts yield U concentrations up to 60 $\mu\text{g/g}$;
 163 garnet/melt partitioning coefficients are non-zero, demonstrating that garnet does not
 164 completely reject U during formation (Hauri et al., 1994; Van Westrenen et al., 1999).

165 In addition to experimental studies documenting the presence of U in the lattice,
 166 mineralogical mechanisms for U-incorporation have also been articulated. Structural modelling

167 of ferrite garnet, in which the Z-site Si is partially replaced by Fe, indicates that the resulting
 168 lattice distortion permits weight-percent U concentrations, in agreement with the natural
 169 occurrence of elbrusite ($\text{Ca}_3(\text{Zr}_{1.5}\text{U}_{0.5}^{6+})\text{Fe}_3^{3+}\text{O}_{12}$), a ferrite garnet in which U is a major element
 170 (Galuskina et al., 2010; Rak et al., 2011). One possible mechanism for U incorporation is the
 171 type of co-substitution found in elbrusite of U^{6+} with a 2+ species at the Y- and Z-sites of
 172 schorlomite group garnet; schorlomite itself ($\text{Ca}_3\text{Ti}_2(\text{SiO}_4)(\text{Fe}^{3+}\text{O}_4)_2$) forms a solid solution
 173 with the silicate garnet group (Grew et al., 2013). This hypothesized mechanism makes the
 174 useful prediction that U should co-occur with Ti or Zr, and Fe^{3+} in garnet group minerals,
 175 although these need only occur in trace quantities as only trace quantities of U are required for
 176 U-Pb analysis. However, as Pb may directly substitute for Fe^{2+} , Mn, Ca, and Mg in the garnet
 177 group X-site (subject to ionic radius constraints), it follows that initial U/Pb ratios during
 178 crystallization may be undesirably low unless Pb has been sequestered in another phase (e.g.,
 179 K-feldspar), or bulk rock U/Pb ratios are high (e.g., garnet crystallising in mantle rocks).
 180 Additionally, as with any U-host, garnet is also amenable to fission track and (U-Th-Sm)/He
 181 dating, although these lower-temperature thermochronometers have seen limited use (Aciego
 182 et al., 2003; Haack & Potts, 1972).

183 Early garnet U-Pb studies employed low-throughput bulk solution analyses, which also
 184 rendered screening for U-hosting inclusions challenging (e.g., Burton et al., 1995; Mezger et
 185 al., 1989). Recent studies employing laser ablation inductively coupled plasma mass
 186 spectrometry (LA-ICPMS) have pioneered the use of large spots to compensate for typically
 187 low U concentrations (Gevedon et al., 2018; Millonig et al., 2020; Salnikova et al., 2018, 2019;
 188 Seman et al., 2017; Yang et al., 2018). Together with identification of matrix-matched
 189 reference materials, this approach has enabled *in-situ* garnet U-Pb analysis. *In-situ* Lu-Hf
 190 analysis, previously hampered by insurmountable isobaric interference of ^{176}Lu on ^{176}Hf , has
 191 been enabled by use of an online mass-filtered reaction cell, (LA-ICPMS/MS) which mass-
 192 shifts ^{176}Hf by reaction with ammonia to form an interference-free higher-mass polyatomic ion
 193 (Simpson et al., 2021; Woods, 2016). *In-situ* analysis enables the high analytical throughput
 194 necessary for routine detrital provenance analysis; if a quadrupole instrument capable of rapid
 195 peak jumps is employed, co-monitoring of relevant elemental masses (eg Zr, Ti, P, LREE)
 196 during analysis also enables efficient screening for U- or Lu-hosting inclusions.

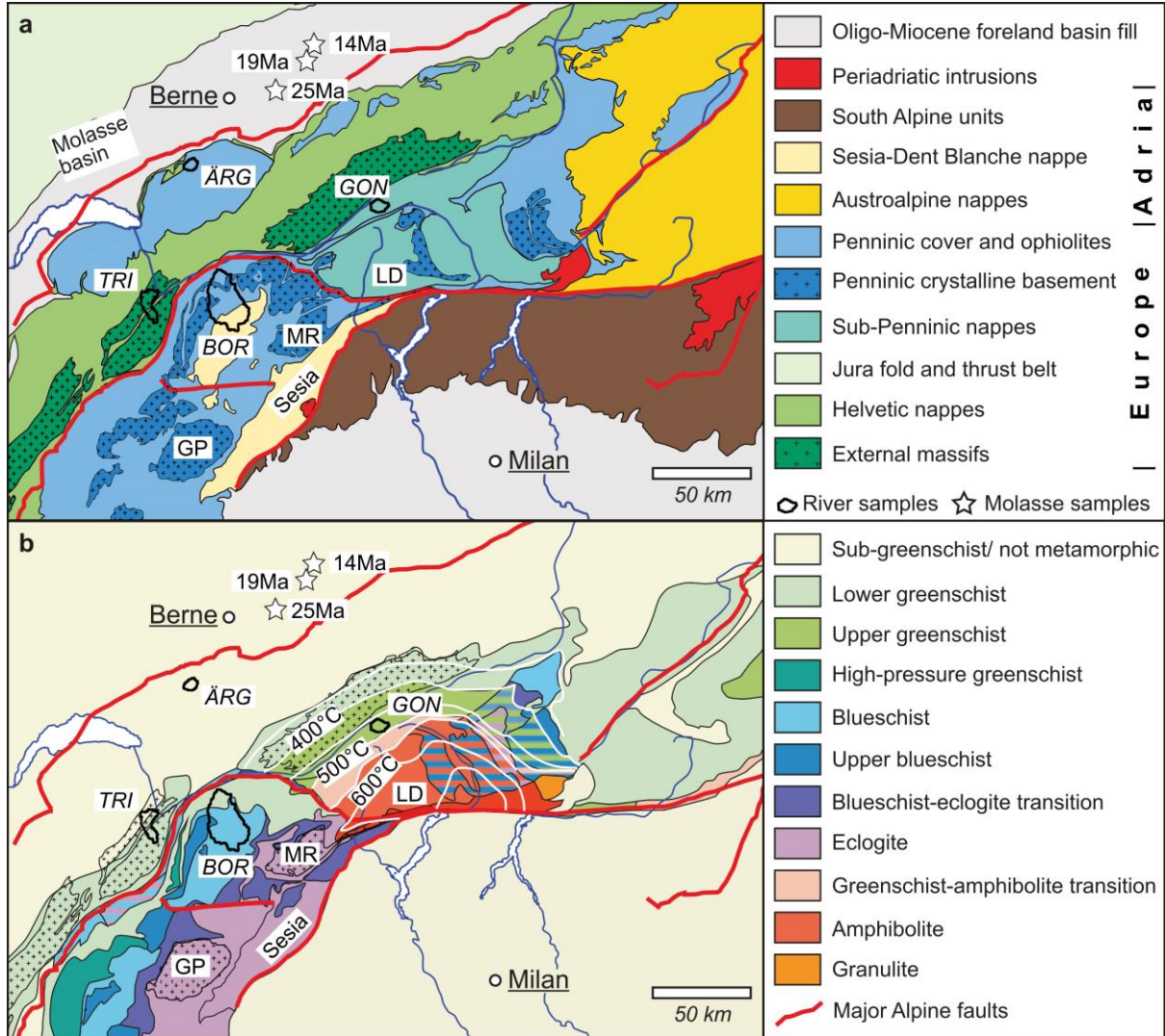
197 Here, we present results from U-Pb and Lu-Hf double-dating, acquired by LA-Q-
 198 ICPMS/(MS) for detrital garnet recovered from the Oligo-Miocene pro-foreland basin of the
 199 European Alps, as well as modern Alpine river bedload. We integrate these with Raman
 200 spectroscopic data and discuss the implications for Alpine tectonics and metamorphism, as well
 201 as the future scope of detrital garnet geochronometry.

202

203 1.3 Geological background of the study area

204 A detailed review of the geological evolution of the eastern Alps is beyond the scope
 205 of this study and the following section is intended only as a brief synopsis. Readers are directed
 206 elsewhere for in-depth discussion (Handy et al., 2010, 2015; Schmid et al., 2008; Stampfli &
 207 Hochard, 2009). Following the prolonged Variscan orogenic cycle (c. 480-290 Ma; Matte,
 208 2001), development of Neotethyan oceanic basins (including the Piedmont-Liguria and Meliata
 209 oceans) led to the separation of Africa from Europe during Late Triassic to Jurassic time,
 210 producing an intervening assemblage of continental microplates and ocean basins.
 211 Reconstructions of this complex tectonic mosaic remain subject to debate, but recent studies
 212 show consensus that the Adria microplate was the southernmost microplate, remained
 213 kinematically linked to Africa, and was separated from the adjacent microcontinent to the
 214 north, termed Alcapia, by a shear zone rather than an ocean basin (Handy et al., 2010, 2015).

215 **Figure 1.** Location map showing (a) tectonic affiliation and (b) metamorphic grade attained
 216 during the Alpine orogen, after Bousquet et al. (2012a,b). Internal massifs: GP – Gran Paradiso;
 217 MR – Monte Rosa; and LD – Lepontine dome and Gotthard nappe. Modern catchments
 218 (*italicised labels*): TRI – Trient; BOR – Borgne; ÄRG – Ärgera; and GON – Goneri. White
 219 stars indicate molasse sampling sites, with deposition ages.
 220



221

222 Shortening of the Adria-Europe tectonic system led to the mid-Cretaceous Eoalpine
 223 event (c. 140-85 Ma; Handy et al., 2010), comprising partial intra-continental subduction of
 224 Alcapia beneath Adria, followed by accretion. Post-Eoalpine, shortening of the Adria-Europe
 225 system was accommodated by subduction of the Piedmont-Ligurian ocean north of Adria
 226 (Handy et al., 2010), culminating in the Alpine orogen (c. 48-15 Ma). The Eoalpine is restricted
 227 to units east of the Arosa Zone, with the exception of the autochthonous Sesia-Dent Blanche
 228 units of the western Alps. The central and western Alps are characterised by broadly orogen-
 229 parallel metamorphic zones, and include twin parallel chains (internal and external) of
 230 crystalline basement massifs (Fig.1). The External Massifs comprise polymetamorphic
 231 gneisses which attained amphibolite-granulite facies during the Eo-Variscan and Variscan
 232 orogens (c. 480-290 Ma; Matte, 2001) followed by Permo-Triassic magmatism and
 233 metamorphism (c. 290-245; (Schuster & Stüwe, 2008), but experienced only moderate (sub-
 234 greenschist to greenschist-facies) Alpine metamorphism (Bousquet et al., 2012a). The Internal
 235 Massifs experienced eclogite- to amphibolite-facies grade metamorphism during the Alpine.
 236 Alpine-age HP metamorphism up to eclogite-facies grade occurred between c. 37-30 Ma in the
 237 Internal Massifs; and at c. 48-42 Ma in the surrounding Penninic metasedimentary and meta-
 238 ophiolitic units (Liatì et al., 2009; Beltrando et al., 2010). The Lepontine Dome subsequently
 239 experienced an amphibolite-facies Barrovian overprint from c. 32-27 Ma which was terminated
 240 by rapid exhumation between c. 22-15 Ma (Boston et al., 2017; Janots et al., 2009).

241

242 **2 Materials and Methods**

243 2.1 Sampling strategy

244 Here, we report data for samples collected both from the bedload of modern rivers
 245 draining small, quasi-monolithologic catchments, as well as from the Oligo-Miocene pro-
 246 foreland molasse basin. These samples were originally collected by Stutenbecker et al. (2017;
 247 2019), who reported major element chemistry acquired using energy-dispersive X-ray
 248 spectrometry and electron microprobe analysis (Fig.2). Sample locations are indicated on
 249 Figure 1 and reported in Table 1. The 63-250 μm size fraction was targeted for garnet
 250 separation.

251

252 2.2 Garnet U-Pb and trace-element analysis by LA-Q-ICPMS

253 Analyses were conducted at the National Centre for Isotope Geochemistry (NCIG) at
 254 University College Dublin using a Teledyne Cetac Analyte G2 ArF 193 nm excimer
 255 nanosecond laser ablation system equipped with a HelEx II two-volume cell, coupled to a
 256 ThermoScientific iCAP Qc quadrupole ICPMS. Masses monitored comprised ^{25}Mg , ^{27}Al , ^{29}Si ,
 257 ^{31}P , ^{43}Ca , ^{49}Ti , ^{53}Cr , ^{55}Mn , ^{57}Fe , ^{60}Ni , ^{89}Y , ^{91}Zr , ^{139}La , ^{140}Ce , ^{141}Pr , ^{146}Nd , ^{147}Sm , ^{153}Eu , ^{157}Gd ,
 258 ^{159}Tb , ^{163}Dy , ^{165}Ho , ^{166}Er , ^{169}Tm , ^{172}Yb , ^{175}Lu , ^{177}Hf , ^{202}Hg , ^{204}Pb , ^{206}Pb , ^{207}Pb , ^{208}Pb , ^{232}Th ,
 259 and ^{238}U . A spot size of 75 μm was employed; further analytical parameters are fully reported
 260 in supplementary table S1. Spikes of P, Ti, Y, Zr, or LREE masses in the time-resolved data
 261 were used to identify and exclude U-hosting inclusions during data reduction (supplementary
 262 Fig.S1). Conventional sample-standard bracketing was employed, with Odikhincha garnet
 263 (Salnikova et al., 2019) used as the primary reference material to correct for intra-session
 264 analytical drift, mass bias, and downhole fractionation. Data reduction employed the
 265 VisualAge_UComPbine data reduction scheme in Iolite 3 (Chew et al., 2014; Paton et al.,
 266 2011). Ages were corrected for common-Pb using the ^{207}Pb method, implemented using the
 267 iterative approach of Mark et al. (2016) which employs the terrestrial Pb-isotope evolution
 268 model of Stacey & Kramers (1975). Age calculations were performed using Isoplot (Ludwig,

269 **Table 1.** Samples used in this study, taken from (Stutenbecker et al., 2017; 2019). MRS –
 270 modern river sediment; UFM – upper fluvial molasse; UMM – upper marine molasse; LFM –
 271 lower fluvial molasse. Deposition ages from magnetostratigraphy of Schlunegger et al. (1996).

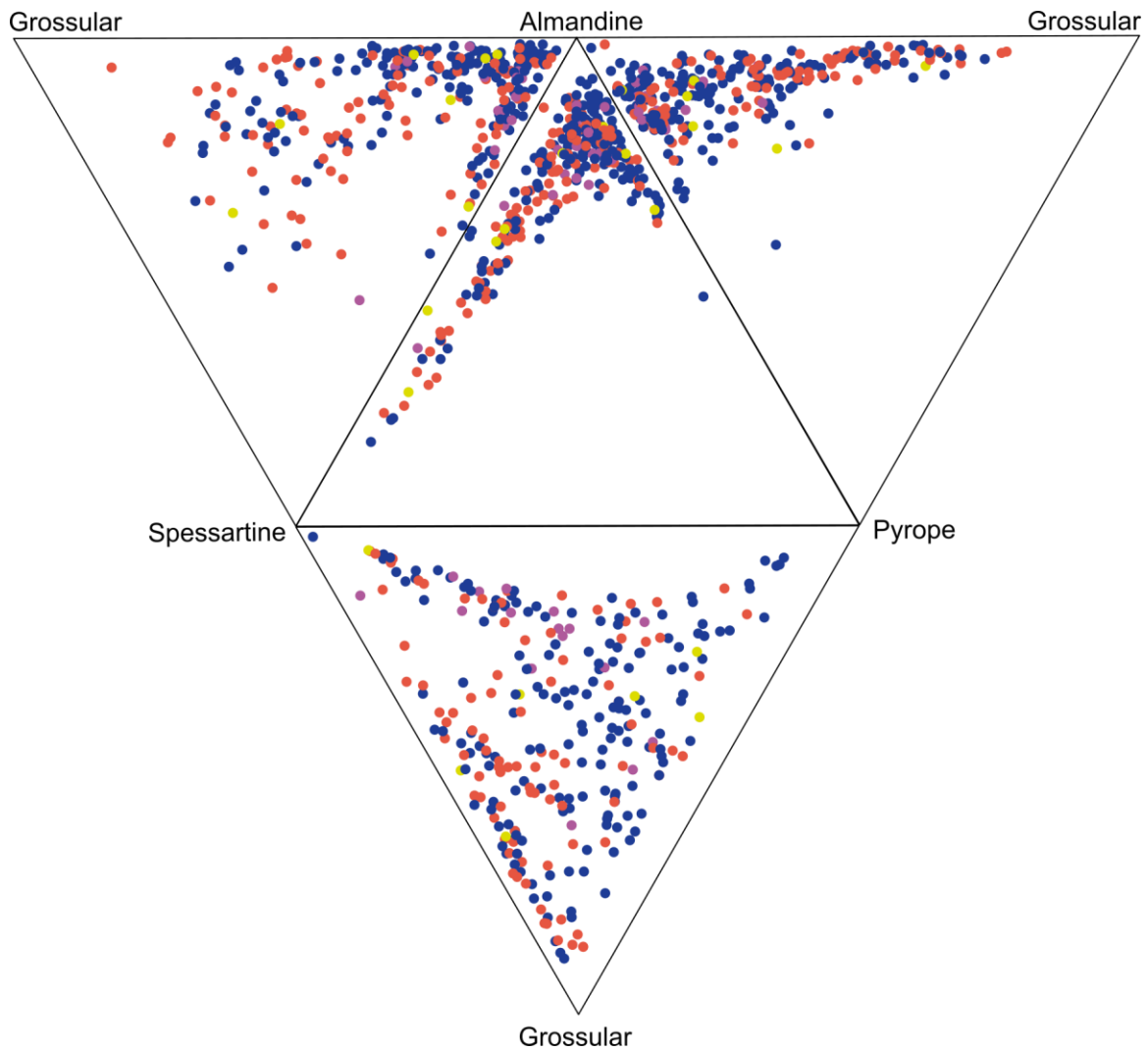
272

Sample	Type	Lat	Long	Description	Deposition age (Ma)	Principal units in catchment
LS2017-3	Molasse bedrock	47.0057	7.9713	UFM - Napf	14	-
LS2018-5	Molasse bedrock	46.9391	7.9508	UMM - Luzern	19	-
LS2016-18	Molasse bedrock	46.7746	7.7324	LFM - Thun	25	-
LS2018-12	MRS	46.7203	7.2455	Ärgera catchment	-	Gurnigel flysch
LS2014-19	MRS	46.2242	7.4072	Borgne catchment	-	St Bernard-Combin-Dent Blanche nappes
LS2014-29	MRS	46.5330	8.3574	Goneri catchment	-	Gotthard nappe
LS2014-37	MRS	46.1323	7.0463	Trient catchment	-	Mont Blanc - Aiguilles Rouges external crystalline massif

273

274 **Figure 2.** Compositions of garnet analysed in this study, from Stutenbecker et al. (2017; 2019).
275 Andradite-rich garnets are excluded (n = 2). Yellow – double-dated; magenta – acceptable Lu-
276 Hf age only; purple – acceptable U-Pb age only; blue – no acceptable age recovered.

277



278

279 2012). As many analyses were discordant due to the incorporation of common-Pb during
 280 crystallization, a discordance filter was not applied. However, many analyses exhibited
 281 undesirably high age uncertainty. An uncertainty filter was therefore applied following the
 282 approach of Chew et al. (2020), such that:

$$283 \quad 2\sigma(\%) \text{ limit} = (5 \times \text{age}^{-0.5}) \times 100$$

284 Afrikanda, Dashkesan, and Chikskii garnets were used as secondary reference materials
 285 and treated as unknowns throughout the data reduction process (reference U-Pb TIMS ages
 286 377 ± 3 Ma, 147 ± 2 Ma, and 492 ± 2 Ma respectively; Salnikova et al., 2018; Salnikova et al.,
 287 2019; Stifeeva et al., 2019). Afrikhanda yielded a lower-intercept U-Pb age of 368.1 ± 2.6 Ma
 288 (MSWD = 1.2, n = 51), and Dashkesan 146.0 ± 1.3 Ma (MSWD = 0.92, n = 50); both are
 289 slightly discordant. Chikskii analyses are over-dispersed (MSWD = 3.3) and show signs of
 290 both Pb-loss and common-Pb incorporation, so no meaningful age can be reported; this is in
 291 agreement with a previous report that the U-Pb system in Chikskii garnet is over-dispersed
 292 (O'Sullivan et al., 2023).

293 Trace element data were also reduced in Iolite using the Trace Elements DRS,
 294 employing ^{29}Si as an internal standard to correct for yield variation. The primary reference
 295 material was NIST612. As no garnet trace element reference material was available, the
 296 komatiite glass GOR-132 was employed as a secondary reference material and treated as an
 297 unknown (Jochum et al., 2006). Reference values typically reproduced within 5% despite many
 298 being present at ng/g concentrations; an exception was Fe which was likely affected by a
 299 polyatomic Ca-based interference (e.g., Malinovsky et al., 2003). This was aggravated by the
 300 unnaturally high reference Ca/Fe ratio in the synthetic NIST glass. U-Pb and trace-element data
 301 are fully reported in supplementary table S2.

302

303 2.3 Garnet Lu-Hf and trace-element analysis by LA-Q-ICPMS/MS

304 A subset of 172 grains where sufficient material remained after U-Pb ablation were
 305 selected for Lu-Hf analysis. Analyses were conducted at Adelaide Microscopy, The University
 306 of Adelaide, using a RESOLUTION 193 nm laser ablation system (Applied Spectra) with a S155
 307 sample chamber (Laurin Technic), coupled to an Agilent 8900x tandem mass spectrometer
 308 (ICPMS/MS). The method involves the addition of NH_3 (supplied as a 1:9 NH_3 :He mix for
 309 safety reasons) into the reaction cell of the mass spectrometer (at a rate of 3 mL min^{-1}) to
 310 promote efficient formation of the $\text{Hf}(\text{NH})(\text{NH}_2)(\text{NH}_3)_3^+$ reaction product as a direct proxy
 311 for ^{176}Hf . Equivalent reaction products for isobars ^{176}Lu and ^{176}Yb are negligible, allowing
 312 ^{176}Hf and ^{176}Lu to be effectively separated and measured free from isobaric interferences
 313 (Simpson et al., 2021; 2022; Glorie et al., 2023a). Following Simpson et al. (2021), $^{176+82}\text{Hf}$
 314 was measured as a proxy for ^{176}Hf ; ^{175}Lu was measured as a proxy for ^{176}Lu , and $^{178+82}\text{Hf}$ was
 315 measured as a proxy for ^{177}Hf . Isotope ratios were calculated in LADR (Norris and
 316 Danyushevsky, 2018) using NIST 610 as a primary standard (Nebel et al., 2009), and corrected
 317 for matrix-induced fractionation using Hogsbo garnet (1029 ± 1.7 Ma; Romer and Smeds,
 318 1996; Simpson et al., 2021). Resulting Lu-Hf dates were calculated as 2-point (inverse)
 319 isochron ages in IsoplotR (Vermeesch, 2018), where the second point comprised an initial
 320 $^{177}\text{Hf}/^{176}\text{Hf}$ anchor of 3.55 ± 0.05 , which spans the entire range of initial $^{177}\text{Hf}/^{176}\text{Hf}$ ratios of
 321 the terrestrial reservoir (e.g., Spencer et al., 2020; Glorie et al., 2023a). The obtained inverse
 322 isochron age for secondary reference material BP-1 garnet was 1752 ± 21 Ma (2σ uncertainty
 323 including propagated uncertainty from Hogsbo) is in good agreement with previously
 324 published Lu-Hf dates (1745 ± 14 Ma and 1744 ± 13 Ma; Simpson et al., 2023 and Glorie et
 325 al., 2023b, respectively). The same uncertainty filter applied to the U-Pb ages was employed.

326 Analytical parameters are fully reported in supplementary table S1. Lu-Hf and trace-
 327 element data are fully reported in supplementary table S2.

328

329 2.4 Garnet composition by Raman spectroscopy

330 A subset of garnets ($n = 45$), including those grains yielding acceptable U-Pb or Lu-Hf
 331 ages where sufficient material remained after ablation, was selected for Raman spectroscopic
 332 analysis. The objective was to assess whether any Raman fingerprint could be used to rapidly
 333 and non-destructively identify grains amenable to dating. This Raman signature is archived in
 334 the entire spectrum as a combination of the Si-O stretching modes represented by “peak 6” (the
 335 main high-frequency band in the $870\text{--}927\text{ cm}^{-1}$ range of Bersani et al., 2009), OH stretching
 336 signals of the OH groups, and laser-induced luminescence bands.

337 Raman spectra of garnet grains were collected at the Laboratory for Provenance Studies
 338 (University of Milano-Bicocca, Italy) using a Renishaw inVia confocal Raman spectroscope,
 339 equipped with a Leica DM2500 microscope. Non-polarized micro-Raman spectra were
 340 obtained in nearly backscattered geometry, with a green 532 nm line, solid-state laser, with a
 341 spectral resolution of $\pm 0.5\text{ cm}^{-1}$, and power $\leq 10\text{ mW}$ at the sample. Before each experimental
 342 session, the system was calibrated using a silicon wafer, having its Raman peak at 520.6 ± 0.3
 343 cm^{-1} . A 50x LWD (long working distance) objective or, when applicable, a 20x objective were
 344 used. The acquisition of each spectrum was set at 1 second of exposure, 100% of laser power
 345 and 30 accumulations. Firstly, the analytical region was centered at 1090 cm^{-1} (corresponding
 346 to a $146\text{--}1912\text{ cm}^{-1}$ spectrum range) in order to detect the six characteristic Raman peaks of
 347 garnets, following Bersani et al. (2009). The spectra were elaborated using a Renishaw
 348 Windows®-based Raman Environment (WiRE, v. 4.4) software for determining the Raman
 349 frequencies of the peaks. Secondly, the analytical region was centered at 3700 cm^{-1} , to observe
 350 any Raman bands related to occurrence of OH groups. Raman luminescence fingerprint was
 351 also analyzed in the high frequency region centered at 4300 cm^{-1} . Raman spectroscopic data
 352 are fully reported in supplementary table S3.

353

354 3 Results

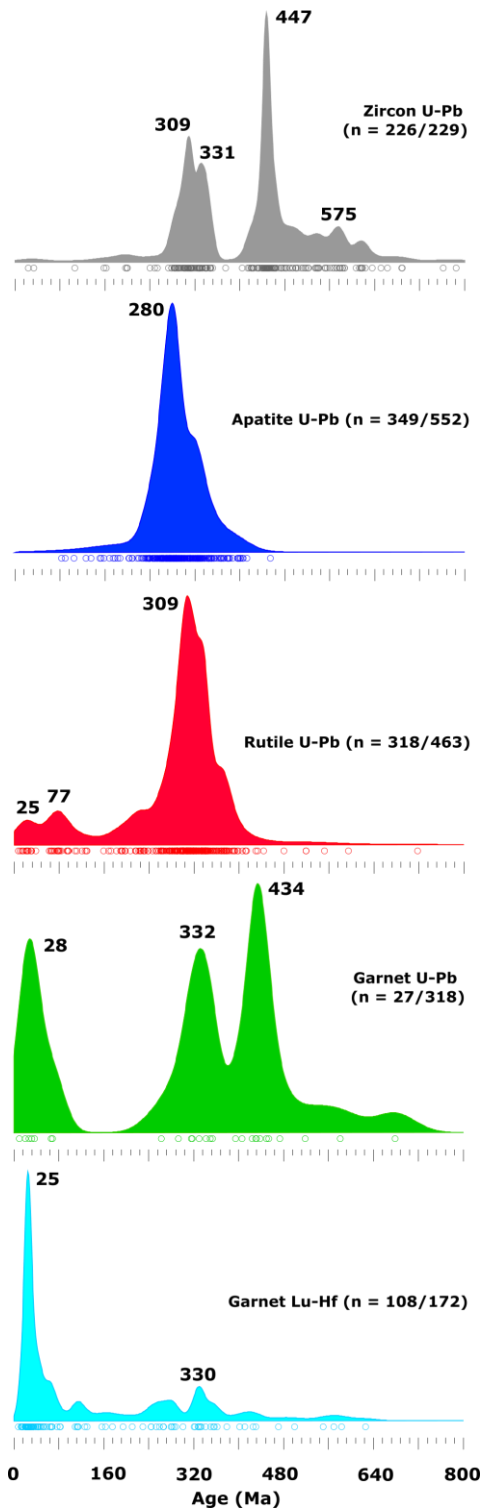
355 Age spectra for all analysed garnets are shown in Fig. 3. The Lu-Hf data yield a major
 356 modal age peak at c. 25 Ma, plus a subordinate peak at c. 330 Ma; the U-Pb data yield
 357 corresponding peaks at c. 28 Ma and c. 332 Ma, plus a peak at c. 434 Ma. 27 acceptable U-Pb
 358 and 108 acceptable Lu-Hf ages were obtained, representing success rates of 8% and 63%
 359 respectively. Raman data showed no correlation with whether an acceptable U-Pb or Lu-Hf
 360 age could be recovered, so are not discussed further.

361

362 4 Discussion

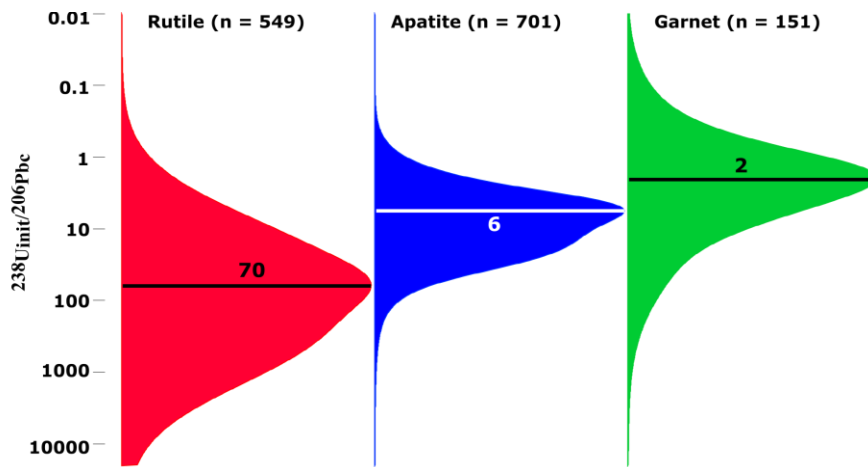
363 Garnet U-Pb age recovery is poor, likely due to low initial U/Pb during crystallisation.
 364 As shown in Fig. 4, garnet in this study is not significantly enriched in U relative to Pb during
 365 crystallization, unlike other common-Pb hosting geochronometers (e.g., rutile and apatite).
 366 Ideally the U-hosting phase effectively excludes common-Pb during crystallization (e.g.,
 367 zircon), but at least some degree of U enrichment is required to permit sufficient ingrowth of
 368 radiogenic Pb over geologically relevant timescales. Lu-Hf age recovery is considerably better,
 369 but still hampered by relatively low Lu concentrations and the relative youthfulness of the
 370 Alpine orogen which reduces the time for ingrowth of ^{176}Hf . There is no systematic relationship
 371

372 **Figure 3.** Kernel density estimates for zircon, apatite, rutile, and garnet U-Pb ages, and garnet
 373 Lu-Hf ages. Zircon data are from Honegg-Napf molasse samples of Zimmermann et al. (2018),
 374 corresponding to Thun-Napf samples of this study; apatite and rutile data are from Honegg-
 375 Napf molasse samples of Mark et al. (2018); and garnet data are from this study. Density plots
 376 generated using DensityPlotter (Vermeesch, 2012). Data are filtered after approach of Chew et
 377 al. (2020), except for zircon which are filtered using a concordance probability threshold as
 378 described by Zimmerman et al. (2018); n = number of acceptable ages/total analyses. A small
 379 number of ages >800 Ma are excluded for clarity (17 zircon; 1 apatite; 0 rutile; 1 garnet U-Pb;
 380 and 1 garnet Lu-Hf).



381

382 **Figure 4.** Distribution and modal values of initial $^{238}\text{U}/^{206}\text{Pb}_c$ ratios at time of crystallization,
383 calculated for Alpine rutile, apatite, and garnet. Rutile and apatite data are from Mark et al.
384 (2018). Garnet data are from this study, and include all analyses for which a finite age could
385 be calculated, regardless of uncertainty.
386



387

388 between garnet composition and whether or not an acceptable age could be obtained, in
 389 agreement with the Raman observations (Fig. 5).

390 4.1 Interpretation of detrital garnet ages

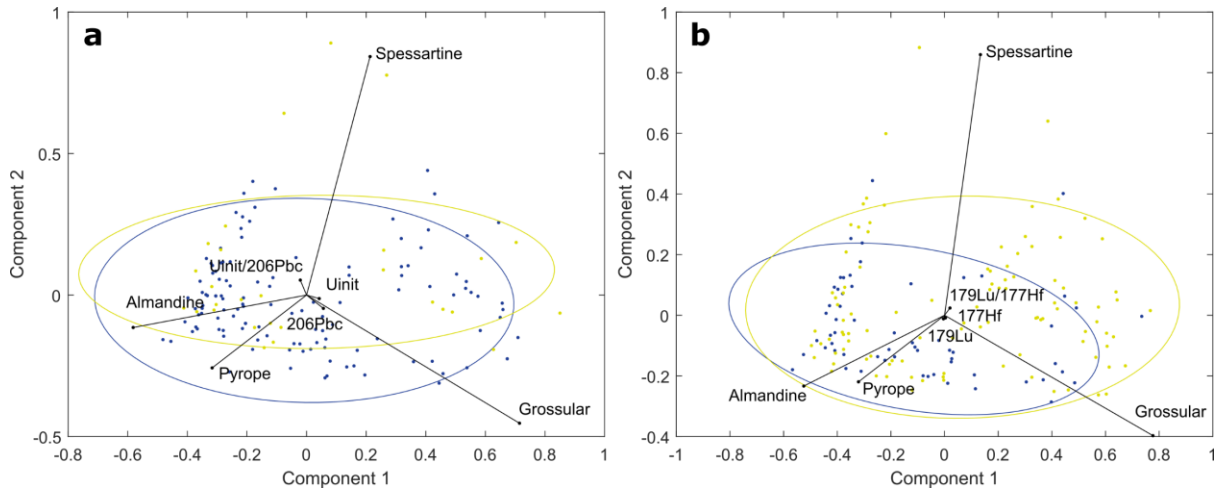
391 The observed garnet U-Pb and Lu-Hf age peaks fit well with known hinterland
 392 tectonometamorphic events. The c. 25-28 Ma age peak records the Barrovian overprint in the
 393 Lepontine Dome (Boston et al., 2017; Janots et al., 2009; Liati et al., 2009). The c. 330-332
 394 Ma age peak records Variscan metamorphism during the collision of Laurussia and Gondwana,
 395 which is widely preserved in polycyclic Alpine crystalline bedrock (e.g., von Raumer et al.,
 396 2009). The c. 434 Ma U-Pb peak records a Siluro-Ordovician metamorphic event documented
 397 in polycyclic units of the external massifs (Schulz & von Raumer, 2011), probably caused by
 398 docking of Armorica and Gondwana (Matte, 2001). Preservation of pre-Alpine detrital garnet
 399 in sedimentary units incorporated into the Alpine orogen and subjected to blueschist facies
 400 metamorphism has also been documented (Manzotti & Ballèvre, 2013).

401 However, the garnet U-Pb and Lu-Hf age spectra clearly differ, with the U-Pb system
 402 preserving more pre-Alpine ages. It is also important to consider that most garnets analysed
 403 here did not yield acceptable ages for both systems; therefore, some of the garnets yielding
 404 Carboniferous and Silurian U-Pb ages could be from sources which were not strongly affected
 405 by the Alpine orogen or which were otherwise shielded, and might have yielded compatible
 406 Lu-Hf ages had sufficient Lu been present. Nonetheless, as previously observed for other
 407 phases (e.g., the U-Pb and Lu-Hf systems in apatite; Glorie et al., 2022), garnet ages obtained
 408 from the same sample using multiple dating methods need not always agree within analytical
 409 uncertainty (e.g., Smit et al., 2013). Such disagreement is expected where radioisotope systems
 410 hosted in the same phase have differing diffusivities. Other causes of over-dispersion may
 411 include inclusions and parent zonation during geologically prolonged or polyphase mineral
 412 growth. Note that these mechanisms are not mutually exclusive. Where *in-situ* analysis is
 413 employed, as here, inclusions are readily detected and excluded by co-analysis of elements
 414 stoichiometric to the phases. Parent isotope zonation effects may be induced either by Raleigh
 415 fractionation (Kohn, 2009) or by polyphase growth. However, in detrital studies, the small age
 416 offsets caused by fractionation effects may be negligible where the objective is to distinguish
 417 between geological events well separated in time, e.g., different orogenies. Polyphase growth
 418 recording multiple orogenic events is likely to be less important in garnet than in more
 419 refractory geochronometers (e.g., the U-Pb system in zircon) because relict or detrital garnet is
 420 thought to seldom survive diagenesis and the early stages of prograde metamorphism (Garzanti
 421 et al., 2018; Cave et al., 2015; Manzotti & Ballèvre, 2013). However, inherited garnet which
 422 is retained in polycyclic crystalline bedrock without being released to the sedimentary system
 423 may record multiple metamorphic events (e.g., Walker et al., 2020; Argles et al., 1999). Thus,
 424 although anticorrelated U and Lu zoning in garnet has been documented (Raimondo et al.,
 425 2017), it is unlikely to be a widespread cause of significantly different U-Pb and Lu-Hf ages.

426 To assess whether the different U-Pb and Lu-Hf age spectra arise from diffusivity, we
 427 calculate the closure temperatures for both systems (Dodson, 1973) in Matlab®. The diffusivity
 428 of Lu and Hf has recently been experimentally re-evaluated in gem-quality natural spessartine
 429 garnet (Bloch et al., 2015, 2020). Unusually, both parent and daughter elements are proposed
 430 to diffuse at geologically reasonable cooling rates and grain sizes. While the closure
 431 temperature for Hf in garnet is typically > 730 °C, Lu may be mobile at temperatures as low as
 432 600-700 °C for grain radii < 100 µm, provided cooling rates are below c. 1 °C/Ma (Fig. 6a &
 433 b). However, at the low concentrations typical in natural garnet, significant Lu diffusion was
 434 observed in experiments at atmospheric pressure but not where experimental pressures
 435 exceeded 1 GPa (Bloch et al., 2020). As experiments at intervening pressures were not

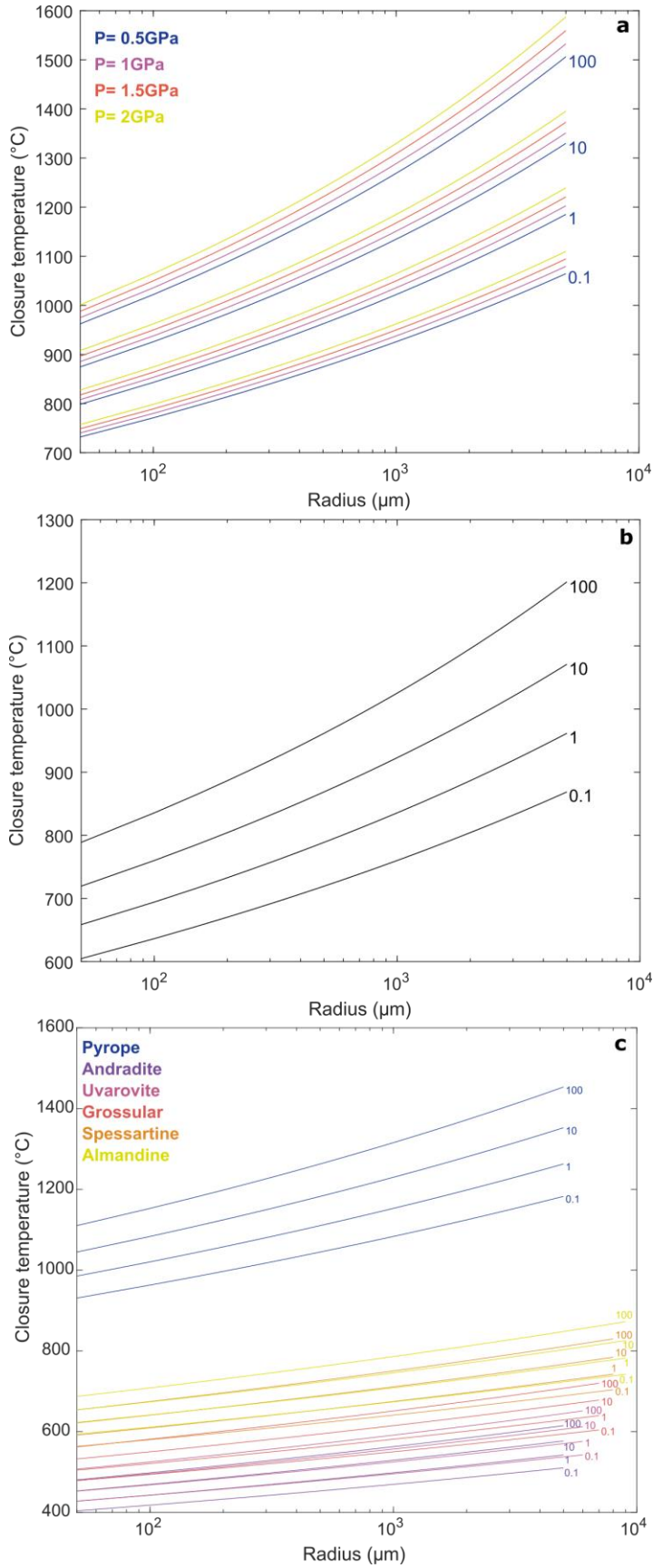
436 **Figure 5.** Principle component analysis plots illustrating the lack of correlation between garnet
 437 composition and age recovery (yellow – age obtained; blue – no age obtained) for (a) U-Pb
 438 and (b) Lu-Hf.

439



440
 441
 442

443 **Figure 6.** Closure temperature estimates for Hf (a), Lu (b), and Pb (c) in garnet, for cooling
 444 rates of 0.1 to 100 °C Ma⁻¹.



445

446 performed it is unclear whether significant Lu diffusion may be expected at geologically
447 plausible PT conditions. The documented preservation of oscillatory Lu zoning in garnet
448 growing during prograde conditions $> 600\text{ }^{\circ}\text{C}$ and $< 1\text{ GPa}$ suggests Lu diffusion in geologically
449 relevant PT conditions may be less significant than experimental data suggest (Guilmette et al.,
450 2018). A pressure control was more definitively documented for Hf diffusivity, but the effect
451 is relatively minor: a 1.5 GPa increase in pressure increases closure temperature by $< 8\%$
452 (Bloch et al., 2020). A dependence on Si activity is even more minor and is not considered
453 here.

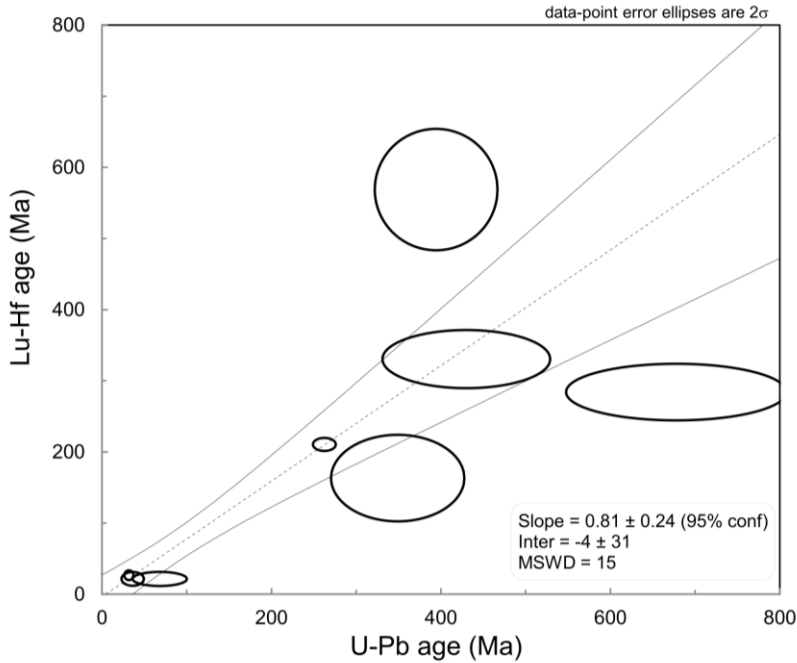
454 For the U-Pb system in garnet, experimental diffusivity data are unfortunately not
455 available and empirical data are limited. Therefore, we use Pb diffusivity documented in other
456 phases and the empirical relationship between ionic porosity and diffusivity to estimate closure
457 temperatures (Dahl, 1997; Zhao & Zheng, 2007). The resulting estimates show a strong
458 compositional control, with the U-Pb system in pyrope having very high closure temperatures
459 (Fig. 6c). As the closure estimates presented here are for pure end-members, it is not clear how
460 to quantify closure temperature for more commonly observed intermediate garnet
461 compositions. However, the majority of garnets analysed in the study are almandine-
462 dominated, which is the second most retentive end-member for Pb after pyrope. Thus, garnets
463 dominated by almandine-pyrope conceivably have higher closure temperatures for U-Pb than
464 for Lu-Hf, especially at low pressures where Lu may be mobile. Unfortunately, it is not possible
465 to calculate Lu-Hf closure temperatures in other garnet end-members for direct comparison
466 using the ionic porosity model, as Hf diffusivity has been determined only in a small number
467 of phases, some of which exhibit very similar diffusivity (almandine, forsterite, rutile,
468 spessartine, and zircon; Bloch et al., 2015, 2020; Cherniak, 2003; Cherniak et al., 2007;
469 Jollands et al., 2014). However, measured diffusivities for these minerals do not display the
470 linear relationship to ionic porosity identified by Zhao & Zheng (2007), and REE and Hf
471 diffusivity was not observed to vary significantly between almandine and spessartine garnet
472 (Bloch et al., 2015).

473 However, for the small subset ($n = 9$) of garnets analysed here which yielded both
474 acceptable Lu-Hf and U-Pb ages, the ages from both systems define a line with a slope and
475 intercept within uncertainty of one and zero respectively, when plotted together (Fig. 7). The
476 small sample size means that the relationship should be treated with some caution, and some
477 ages are clearly in disagreement. Nonetheless, these double-dated grains suggest that ages
478 obtained from both systems are likely to be in agreement, and do not indicate a systematic
479 tendency for either radioisotope system to yield older ages, which would be expected if one
480 system had significant diffusivity at Alpine metamorphic temperatures.

481 4.2 Relationship of detrital garnet ages to other detrital geochronometers

482 The detrital garnet Lu-Hf and U-Pb ages can also usefully be compared with the age
483 spectra of other detrital geochronometers recovered from the same molasse units (Fig. 3). The
484 Alpine orogen is essentially unrecorded by the U-Pb system in zircon, due to the very limited
485 degree of anataxis which is restricted to the Periadriatic line plutons (e.g., the Bergell and
486 Adamello). Outwith these volumetrically small intrusions, Alpine zircon neocrystallisation is
487 limited to epitaxial overgrowth (Rubatto & Hermann, 2003). The U-Pb system in apatite also
488 yields only a small number of Alpine ages, and is dominated by Variscan metamorphism and
489 post-Variscan magmatism (c. 290 Ma; Cassinis et al., 2011). While Alpine rocks yield
490 abundant apatite, the widespread greenschist to amphibolite facies grade metamorphism of the
491 central Alps is associated with low-U apatite, likely rendering many Alpine-age apatite grains
492 undatable by U-Pb (Henrichs et al., 2019; Malusà et al., 2017). The U-Pb system in rutile does
493

494 **Figure 7.** Age_{U-Pb} vs Age_{Lu-Hf} for double-dated garnets (n = 9) yielding acceptable ages for both
 495 systems. These define a line with a slope and intercept within uncertainty of one and zero,
 496 respectively; however, some ages are not in agreement as indicated by the high MSWD.
 497 Consistent agreement between the two age systems is not necessarily expected given the
 498 differences in closure temperature.



499

500 yield subordinate Alpine age peaks, but at c. 77 Ma and c. 25 Ma; the former likely records
501 Eoalpine metamorphism in the Sesia unit, and the latter likely records cooling through the Pb
502 partial retention zone towards the end of the Lepontine Barrovian overprint. However, the
503 dominant rutile U-Pb age peaks are Variscan.

504 Thus, detrital garnet ages appear strongly biased towards the most recent garnet-
505 crystallising metamorphic event, with fewer pre-Alpine ages than other detrital
506 geochronometers. This is probably due to garnet being much less refractory than rutile or
507 zircon, although polycyclic garnet has been documented (e.g., Argles et al., 1999; Manzotti &
508 Ballèvre, 2013). The U-Pb system in detrital rutile also provides a proxy for metamorphism as
509 rutile rarely forms as a primary igneous mineral (Force, 1980), but the much more refractory
510 nature of rutile means that a larger number of polycyclic grains yielding inherited ages are
511 likely to be analysed as well. Garnet is readily removed from heavy mineral assemblages during
512 diagenesis; in contrast, rutile, together with zircon and tourmaline, is typically among the most
513 persistent heavy minerals (Hubert, 1962). Both garnet and rutile are also likely to break down
514 during the sub-greenschist-facies-grade stages of prograde metamorphism (Cave et al., 2015).
515 Detrital garnet geochronology may thus hold potential as a proxy for the most recent mid-grade
516 metamorphism in the source area, especially for less deeply eroded orogens preserving
517 widespread metapelitic rocks which are likely to be rich in garnet. In this context, mid-grade
518 metamorphic source rocks attain sufficiently high pressures and temperatures to crystallise
519 garnet, but fall short of anataxis and therefore do not crystallise zircon. The PT conditions for
520 the garnet-in isograd will evidently vary considerably depending on rock composition, but
521 temperature estimates between c. 450 – 550 °C for metapelitic rocks are commonly reported,
522 i.e., within the upper-greenschist-facies- and upper-blueschist-facies-grades (e.g., Florence &
523 Spear, 1993). However, spessartine-rich garnet is stabilised in Mn-rich metapelites at
524 temperatures at least as low as 400 °C (White et al., 2014) and potentially as low as 300-350
525 °C (Kennan & Murphy, 1993), showing the importance of integrating garnet composition with
526 age interpretation. These temperatures are lower than typical rutile formation temperatures of >
527 c. 450 °C (Chambers & Kohn, 2012), illustrating that detrital garnet geochronology may be
528 usefully applied to lower-grade orogens which did not extensively crystallise rutile. While such
529 orogens may also be appropriate targets for $^{40}\text{Ar}/^{39}\text{Ar}$ or $^{87}\text{Rb}/^{87}\text{Sr}$ analysis of detrital mica,
530 garnet is less prone to alteration or hydrodynamic fractionation during transport (Garzanti et
531 al., 2008).

532 The similarity of the garnet and rutile Alpine age peaks (c. 28-25 Ma vs c. 25 Ma,
533 respectively) is in reasonable agreement with documented Alpine PT conditions.
534 Pseudosection modelling using average bulk compositions of passive margin pelite and
535 greywacke can be used to approximate global PT stability fields for these phases (Yakymchuk
536 et al., 2018). Such modelling is evidently rather idealized and it is unclear if similar PT stability
537 fields may be expected from metagranitoids, which are widespread in the western and central
538 Alps, or in metasedimentary rocks which significantly deviate from average global
539 compositions. Nonetheless, these models do provide at least some indication of likely mineral
540 PT stability fields. For these bulk compositions, rutile is completely removed between c. 460-
541 670 °C at pressures < 1 GPa, with rutile stability increasing with pressure. In contrast, garnet
542 is present throughout this temperature range. At pressures > 1 GPa, both rutile and garnet are
543 stable (Yakymchuk et al., 2018). Assuming these metasedimentary rock types are reasonable
544 approximations for Alpine source rocks, neocrystalline Alpine rutile and garnet can only yield
545 similar ages if source rocks have equilibrated at peak PT conditions within the rutile stability
546 field, i.e. at < c. 460-670 °C if pressure is < 1 GPa. These values agree reasonably well with
547 documented PT conditions for Alpine Barrovian metamorphism of c. 350-700 C and \leq 0.8 GPa
548 (Todd and Engi, 1997).

549 Additionally, the overlap between Alpine garnet and rutile ages suggests that post-peak
 550 cooling to temperatures below the thermal sensitivity of the U-Pb system in rutile must have
 551 been geologically rapid. Diffusivity of Pb in rutile is well established, with experimental and
 552 empirical studies indicating a partial retention zone of c. 490 – 640 °C for geologically typical
 553 grain sizes and cooling rates (Cherniak, 2000; Kooijman et al., 2010). Thermal sensitivity of
 554 both the U-Pb and Lu-Hf systems in garnet is less well constrained, but considered to be c. 600
 555 - 1050 °C for the almandine-dominated garnets analysed here, of typical detrital grain size (50-
 556 100 µm radius) subjected to geologically common cooling rates (e.g., Bloch et al., 2020;
 557 O’Sullivan et al., 2023; Smit et al., 2013). Therefore, prolonged residence at temperatures >
 558 490 °C would be expected to yield rutile U-Pb ages younger than garnet ages. Similar rutile
 559 and garnet Alpine ages agree with documented rapid cooling of the Lepontine Dome and
 560 southern Aar-Gotthard massif between c. 22-15 Ma (Boston et al., 2017; Janots et al., 2009).

561

562 **5 Conclusions**

563 Both the U-Pb and Lu-Hf isotope systems in garnet are biased towards the youngest
 564 garnet-crystallising metamorphic event in the source area, in agreement with the less refractory
 565 nature of garnet compared to rutile or zircon. Detrital garnet geochronology therefore shows
 566 utility where the objective is to identify sediment sourced from the youngest and, hence, likely
 567 most rapidly exhumed component of an orogen without co-analysis of large numbers of
 568 inherited ages. Age recovery for both systems is not compositionally biased, at least for the
 569 generally almandine-rich garnets analysed here. However, the Lu-Hf system shows
 570 considerably better age recovery than the U-Pb system (8% vs 63%), due to the failure of garnet
 571 to concentrate U relative to Pb during crystallisation. While possible compositional and
 572 pressure controls on both the U-Pb and Lu-Hf system in garnet may complicate age
 573 interpretation, the ability of this study to reproduce the age of Alpine Barrovian metamorphism
 574 indicates that these complexities are generally unimportant. Detrital garnet Lu-Hf dating,
 575 coupled in future with compositional analysis and crystallisation pressure estimates using
 576 thermobarometry (Kohn, 2014) and Zr-in-rutile or –titanite detrital thermometry, may offer
 577 scope for rapid first-order reconstruction of source area pressure-time evolution, especially in
 578 areas difficult to access directly.

579

580 **Acknowledgments**

581 The authors acknowledge financial support from Science Foundation Ireland (Starting
 582 Investigator Research Grant 18/SIRG/5559 to CM), the Australian Research Council (Future
 583 Fellowship FT210100906 to SG), and the Irish Research Council (Government of Ireland
 584 Postdoctoral Fellowship GOIPD/2019/906 to GO’S). NCIG equipment used in this study was
 585 funded by grants from Science Foundation Ireland (13/RC/2092) and the Irish Higher
 586 Education Authority through the Programme for Research at Third Level Institutions, Cycle 5
 587 (PRTL-5). We thank Ekaterina Salnikova for supplying garnet U-Pb reference materials,
 588 Sarah Gilbert for assistance with LA-ICP-MS/MS setup, Matthijs Smit for helpful discussion
 589 on Lu-Hf systematics, reviewers X and Y for constructive comments, and Z for editorial
 590 handling.

591

592 **Open Research Statement**

593 The data reported in this study are fully tabulated in the supplementary materials
 594 accessible at www.doi.org/10.5281/zenodo.7900189. The most recent version of the Iolite

595 software used for U-Pb and trace-element data reduction is available from www.iolite.xyz (a
596 division of Elemental Scientific, Inc.). The LADR software used for Lu-Hf data reduction is
597 available from www.norsci.com. Both data reduction packages are available under proprietary
598 license.

599

600 **References**

- 601 Aciego, S., Kennedy, B. M., DePaolo, D. J., Christensen, J. N., & Hutcheon, I. (2003). U-Th/He age of
602 phenocrystic garnet from the 79 AD eruption of Mt. Vesuvius. *Earth and Planetary Science Letters*,
603 *216*(1–2), 209–219. [https://doi.org/10.1016/S0012-821X\(03\)00478-3](https://doi.org/10.1016/S0012-821X(03)00478-3)
- 604 Andò, S., Garzanti, E., Padoan, M., & Limonta, M. (2012). Corrosion of heavy minerals during weathering and
605 diagenesis : A catalog for optical analysis. *Sedimentary Geology*, *280*, 165–178.
606 <https://doi.org/10.1016/j.sedgeo.2012.03.023>
- 607 Andò, S., Morton, A., & Garzanti, E. (2013). Metamorphic grade of source rocks revealed by chemical
608 fingerprints of detrital amphibole and garnet. *Geological Society, London, Special Publications*, *386*(1),
609 351–371. <https://doi.org/10.1144/SP386.5>
- 610 Argles, T. W., Prince, C. I., Foster, G. L., & Vance, D. (1999). New garnets for old? Cautionary tales from
611 young mountain belts. *Earth and Planetary Science Letters*, *172*.
- 612 Baxter, E. F., & Scherer, E. E. (2013). Garnet geochronology: Timekeeper of tectonometamorphic processes.
613 *Elements*, *9*(6), 433–438. <https://doi.org/10.2113/gselements.9.6.433>
- 614 Beltrando, M., Compagnoni, R., & Lombardo, B. (2010). (Ultra-) High-pressure metamorphism and orogenesis:
615 An Alpine perspective. *Gondwana Research*, *18*(1), 147–166. <https://doi.org/10.1016/j.gr.2010.01.009>
- 616 Bersani, D., Andò, S., Vignola, P., Moltifiori, G., Marino, I. G., Lottici, P. P., & Diella, V. (2009). Micro-
617 Raman spectroscopy as a routine tool for garnet analysis. *Spectrochimica Acta - Part A: Molecular and*
618 *Biomolecular Spectroscopy*, *73*, 484–491. <https://doi.org/10.1016/j.saa.2008.11.033>
- 619 Bloch, E., Ganguly, J., Hervig, R., & Cheng, W. (2015). ¹⁷⁶Lu–¹⁷⁶Hf geochronology of garnet I: experimental
620 determination of the diffusion kinetics of Lu³⁺ and Hf⁴⁺ in garnet, closure temperatures and
621 geochronological implications. *Contributions to Mineralogy and Petrology*, *169*(2).
622 <https://doi.org/10.1007/s00410-015-1109-8>
- 623 Bloch, E., Jollands, M. C., Devoir, A., Bouvier, A. S., Ibañez-Mejia, M., & Baumgartner, L. P. (2020).
624 Multispecies diffusion of yttrium, rare earth elements and hafnium in garnet. *Journal of Petrology*, *61*(7).
625 <https://doi.org/10.1093/petrology/egaa055>
- 626 Boehnke, P., Watson, E. B., Trail, D., Harrison, T. M., & Schmitt, A. K. (2013). Zircon saturation re-revisited.
627 *Chemical Geology*, *351*, 324–334. <https://doi.org/10.1016/j.chemgeo.2013.05.028>
- 628 Boston, K. R., Rubatto, D., Hermann, J., Engi, M., & Amelin, Y. (2017). Geochronology of accessory allanite
629 and monazite in the Barrovian metamorphic sequence of the Central Alps, Switzerland. *Lithos*, *286–287*,
630 502–518. <https://doi.org/10.1016/j.lithos.2017.06.025>
- 631 Burton, K. W., Kohn, M. J., Cohen, A. S., & Keith O’Nions, R. (1995). The relative diffusion of Pb, Nd, Sr and
632 O in garnet. *Earth and Planetary Science Letters*, *133*(1–2), 199–211. [https://doi.org/10.1016/0012-821X\(95\)00067-M](https://doi.org/10.1016/0012-821X(95)00067-M)
- 633
- 634 Bousquet, R., Oberhänsli, R., Schmid, S. M., Berger, A., Wiederkehr, M., Möller, A., Rosenberg, C., Koller, F.,
635 Molli, G., & Zeilinger, G. (2012a). Metamorphic framework of the Alps. *CCGM/CGMW*, scale
636 1:1,000,000.
- 637 Bousquet, R., Schmid, S. M., Zeilinger, G., Oberhänsli, R., Rosenberg, C., Molli, G., Robert, C., Wiederkehr,
638 M., & Rossi, P., (2012b). Tectonic framework of the Alps. *CCGM/CGMW*, scale 1:1,000,000,
- 639 Campbell, I. H., Reiners, P. W., Allen, C. M., Nicolescu, S., & Upadhyay, R. (2005). He – Pb double dating of
640 detrital zircons from the Ganges and Indus Rivers : Implication for quantifying sediment recycling and
641 provenance studies, *237*, 402–432. <https://doi.org/10.1016/j.epsl.2005.06.043>
- 642 Cassinis, G., Perotti, C. R., & Ronchi, A. (2011). Permian continental basins in the Southern Alps (Italy) and
643 peri-mediterranean correlations. *International Journal of Earth Sciences*, *101*(1), 129–157.
644 <https://doi.org/10.1007/s00531-011-0642-6>
- 645 Cave, B., Stepanov, A., Craw, D., Large, R., Halpin, J., & Thompson, J. (2015). Release of trace elements
646 through the sub-greenschist facies breakdown of detrital rutile to metamorphic titanite in the Otago schist,
647 New Zealand. *The Canadian Mineralogist*, *53*, 379–400. <https://doi.org/10.3749/canmin.1400097>
- 648 Chambers, J. A., & Kohn, M. J. (2012). Titanium in muscovite, biotite, and hornblende: Modeling,
649 thermometry, and rutile activities of metapelites and amphibolites. *American Mineralogist*, *97*(4), 543–
650 555. <https://doi.org/10.2138/am.2012.3890>
- 651 Cherniak, D. J. (2000). Pb diffusion in rutile. *Contributions to Mineralogy and Petrology*, *139*, 198–207.

- 652 Cherniak, D. J. (2003). Diffusion in Zircon. *Reviews in Mineralogy and Geochemistry*, 53(1), 113–143.
653 <https://doi.org/10.2113/0530113>
- 654 Cherniak, D. J., Manchester, J., & Watson, E. B. (2007). Zr and Hf diffusion in rutile. *Earth and Planetary
655 Science Letters*, 261(1–2), 267–279. <https://doi.org/10.1016/j.epsl.2007.06.027>
- 656 Chew, D., Petrus, J. A., & Kamber, B. S. (2014). U-Pb LA-ICPMS dating using accessory mineral standards
657 with variable common Pb. *Chemical Geology*, 363, 185–199.
658 <https://doi.org/10.1016/j.chemgeo.2013.11.006>
- 659 Chew, David, O’Sullivan, G., Caracciolo, L., Mark, C., & Tyrrell, S. (2020). Sourcing the sand: Accessory
660 mineral fertility, analytical and other biases in detrital U-Pb provenance analysis. *Earth-Science Reviews*,
661 202(August 2019), 103093. <https://doi.org/10.1016/j.earscirev.2020.103093>
- 662 Christensen, J. N., Rosenfeld, J. L., & DePaolo, D. J. (1989). Rates of Tectonometamorphic Processes from
663 Rubidium and Strontium Isotopes in Garnet. *Science*, 244(4911), 1465–1469.
664 <https://doi.org/10.1126/science.244.4911.1465>
- 665 Connally, G. G. (1964). Garnet ratios and provenance in the glacial drift of western New York. *Science*,
666 144(3625), 1452–1453. <https://doi.org/10.1126/science.144.3625.1452>
- 667 Dahl, P. S. (1997). A crystal-chemical basis for Pb retention and fission-track annealing systematics in U-
668 bearing minerals, with implications for geochronology. *Earth and Planetary Science Letters*, 150(3–4),
669 277–290. [https://doi.org/10.1016/s0012-821x\(97\)00108-8](https://doi.org/10.1016/s0012-821x(97)00108-8)
- 670 DePaolo, D. J., & Wasserburg, G. J. (1976). Inferences about magma sources and mantle structure from
671 variations of ¹⁴³Nd/¹⁴⁴Nd. *Geophysical Research Letters*, 3(12), 743–746.
672 <https://doi.org/10.1029/GL003i012p00743>
- 673 DeWolf, C. P., Zeissler, C. J., Halliday, A. N., Mezger, K., & Essene, E. J. (1996). The role of inclusions in U-
674 Pb and Sm-Nd garnet geochronology: Stepwise dissolution experiments and trace uranium mapping by
675 fission track analysis. *Geochimica et Cosmochimica Acta*, 60, 121–134.
- 676 Dodson, M. H. (1973). Closure temperature in cooling geochronological and petrological systems.
677 *Contributions to Mineralogy and Petrology*, 40(3), 259–274. <https://doi.org/10.1007/BF00373790>
- 678 Duchêne, S., Blichert-Toft, J., Luais, B., Télouk, P., Lardeaux, J. M., & Albarède, F. (1997). The Lu-Hf dating
679 of garnets and the ages of the Alpine high-pressure metamorphism. *Nature*, 387, 586–589.
680 <https://doi.org/10.1038/42446>
- 681 von Eynatten, H., & Dunkl, I. (2012). Assessing the sediment factory: The role of single grain analysis. *Earth-
682 Science Reviews*, 115(1–2), 97–120. <https://doi.org/10.1016/j.earscirev.2012.08.001>
- 683 Florence, F., & Spear, F. (1993). Influences of reaction history and chemical diffusion on P-T calculations for
684 staurolite schists from the Littleton Formation, northwestern New Hampshire. *American Mineralogist*, 78,
685 345–359. Retrieved from [http://pubs.geoscienceworld.org/msa/ammin/article-pdf/78/3-
686 4/345/4218183/am78_345.pdf](http://pubs.geoscienceworld.org/msa/ammin/article-pdf/78/3-4/345/4218183/am78_345.pdf)
- 687 Force, E. R. (1980). The provenance of rutile. *Journal of Sedimentary Petrology*, 50, 485–488.
- 688 Galuskina, I. O., Galuskin, E. V., Armbrusteter, T., Lazic, B., Kusz, J., Dzierzanowski, P., et al. (2010).
689 Elbrusite-(Zr)-A new uranian garnet from the Upper Chegem caldera, Kabardino-Balkaria, Northern
690 Caucasus, Russia. *American Mineralogist*, 95(8–9), 1172–1181. <https://doi.org/10.2138/am.2010.3507>
- 691 Garçon, M., Chauvel, C., France-Lanord, C., Limonta, M., & Garzanti, E. (2014). Which minerals control the
692 Nd – Hf – Sr – Pb isotopic compositions of river sediments? *Chemical Geology*, 364, 42–55.
693 <https://doi.org/10.1016/j.chemgeo.2013.11.018>
- 694 Garzanti, E., Vezzoli, G., Andò, S., Paparella, P., & Clift, P. D. (2005). Petrology of Indus River sands: A key to
695 interpret erosion history of the Western Himalayan Syntaxis. *Earth and Planetary Science Letters*, 229,
696 287–302. <https://doi.org/10.1016/j.epsl.2004.11.008>
- 697 Garzanti, E. & Andò, S. (2007). Plate tectonics and heavy-mineral suites of modern sands. In: Mange, M. A. &
698 Wright, D. T. (eds) *Heavy Minerals in Use*. Elsevier, Amsterdam, *Developments in Sedimentology*, 58,
699 741–763.
- 700 Garzanti, E., Andò, S., & Vezzoli, G. (2008). Settling equivalence of detrital minerals and grain-size
701 dependence of sediment composition. *Earth and Planetary Science Letters*, 273(1–2), 138–151.
702 <https://doi.org/10.1016/j.epsl.2008.06.020>
- 703 Garzanti, E., Resentini, A., Vezzoli, G., Andò, S., Malusà, M. G., Padoan, M., & Paparella, P. (2010a). Detrital
704 fingerprints of fossil continental-subduction zones (axial belt provenance, European Alps). *The Journal of
705 Geology*, 118(4), 341–362. <https://doi.org/10.1086/652720>
- 706 Garzanti, E., Andò, S., France-Lanord, C., Vezzoli, G., Censi, P., Galy, V., & Najman, Y. (2010b).
707 Mineralogical and chemical variability of fluvial sediments. 1. Bedload sand (Ganga-Brahmaputra,
708 Bangladesh). *Earth and Planetary Science Letters*, 299, 368–381.
709 <https://doi.org/10.1016/j.epsl.2010.09.017>

- 710 Garzanti, E., Andò, S., Padoan, M., Vezzoli, G., & El Kammar, A. (2015). The modern Nile sediment system:
711 Processes and products. *Quaternary Science Reviews*, *130*, 9–56.
712 <https://doi.org/10.1016/j.quascirev.2015.07.011>
- 713 Garzanti, E., Andò, S., Limonta, M., Fielding, L., & Najman, Y. (2018). Diagenetic control on mineralogical
714 suites in sand, silt, and mud (Cenozoic Nile Delta): Implications for provenance reconstructions. *Earth-*
715 *Science Reviews*. Elsevier B.V. <https://doi.org/10.1016/j.earscirev.2018.05.010>
- 716 Garzanti, E., Vermeesch, P., Vezzoli, G., Andò, S., Botti, E., Limonta, M., et al. (2019). Congo River sand and
717 the equatorial quartz factory. *Earth-Science Reviews*. Elsevier B.V.
718 <https://doi.org/10.1016/j.earscirev.2019.102918>
- 719 Garzanti, E., Pastore, G., Resentini, A., Vezzoli, G., Vermeesch, P., Ncube, L., et al. (2021). The segmented
720 Zambezi sedimentary system from source to sink: 1. Sand petrology and heavy minerals. *Journal of*
721 *Geology*, *129*(4), 343–369. <https://doi.org/10.1086/715792>
- 722 Gevedon, M., Seman, S., Barnes, J. D., Star, J., & Stockli, D. F. (2018). Unraveling histories of hydrothermal
723 systems via U – Pb laser ablation dating of skarn garnet. *Earth and Planetary Science Letters*, *498*, 237–
724 246. <https://doi.org/10.1016/j.epsl.2018.06.036>
- 725 Glorie, S., Gillespie, J., Simpson, A., Gilbert, S., Khudoley, A., Priyatkina, N., et al. (2022). Detrital apatite Lu–
726 Hf and U–Pb geochronology applied to the southwestern Siberian margin. *Terra Nova*.
727 <https://doi.org/10.1111/ter.12580>
- 728 Glorie, S., Hand, M., Mulder, J., Simpson, A., Emo, R. B., Kamber, B., Fernie, N., Nixon, A., & Gilbert, S.
729 (2023a). Robust laser ablation Lu–Hf dating of apatite: an empirical evaluation. *Geological Society,*
730 *London, Special Publications*, *537*(1). <https://doi.org/10.1144/SP537-2022-205>
- 731 Glorie, S., Mulder, J., Hand, M., Fabris, A., Simpson, A., Gilbert, S. (2023). Laser ablation (in situ) Lu–Hf dating
732 of magmatic fluorite and hydrothermal fluorite-bearing veins. *Geoscience Frontiers*.
- 733 Grew, E. S., Locock, A. J., Mills, S. J., Galuskina, I. O., Galuskin, E. V., & Halenius, U. (2013). Nomenclature
734 of the garnet supergroup. *American Mineralogist*, *98*(4), 785–811. <https://doi.org/10.2138/am.2013.4201>
- 735 Guilmette, C., Smit, M. A., van Hinsbergen, D. J. J., Gürer, D., Corfu, F., Charette, B., et al. (2018). Forced
736 subduction initiation recorded in the sole and crust of the Semail Ophiolite of Oman. *Nature Geoscience*,
737 *11*(9), 688–695. <https://doi.org/10.1038/s41561-018-0209-2>
- 738 Haack, U. K., & Gramse, M. (1972). Survey of garnets for fossil fission tracks. *Contributions to Mineralogy*
739 *and Petrology*, *34*(3), 258–260. <https://doi.org/10.1007/BF00373298>
- 740 Haack, U. K., & Potts, M. J. (1972). Fission track annealing in garnet. *Contributions to Mineralogy and*
741 *Petrology*, *34*(4), 343–345. <https://doi.org/10.1007/BF00373764>
- 742 Handy, M. R., Schmid, S., Bousquet, R., Kissling, E., & Bernoulli, D. (2010). Reconciling plate-tectonic
743 reconstructions of Alpine Tethys with the geological–geophysical record of spreading and subduction in
744 the Alps. *Earth-Science Reviews*, *102*(3–4), 121–158. <https://doi.org/10.1016/j.earscirev.2010.06.002>
- 745 Handy, M. R., Ustaszewski, K., & Kissling, E. (2015). Reconstructing the Alps–Carpathians–Dinarides as a key
746 to understanding switches in subduction polarity, slab gaps and surface motion. *International Journal of*
747 *Earth Sciences*, *104*(1), 1–26. <https://doi.org/10.1007/s00531-014-1060-3>
- 748 Hauri, E. H., Wagner, T. P., & Grove, T. L. (1994). Experimental and natural partitioning of Th, U, Pb and other
749 trace elements between garnet, clinopyroxene and basaltic melts. *Chemical Geology*, *117*(1–4), 149–166.
750 [https://doi.org/10.1016/0009-2541\(94\)90126-0](https://doi.org/10.1016/0009-2541(94)90126-0)
- 751 Henrichs, I. A., Chew, D. M., O’Sullivan, G. J., Mark, C., McKenna, C., & Guyett, P. (2019). Trace element
752 Mn–Sr–Y–Th–REE) and U–Pb isotope systematics of metapelitic apatite during progressive greenschist- to
753 amphibolite-facies Barrovian metamorphism. *Geochemistry, Geophysics, Geosystems*, *20*(8).
754 <https://doi.org/10.1029/2019GC008359>
- 755 Hubert, J. (1962). A zircon-tourmaline-rutile maturity index and the interdependence of the composition of
756 heavy mineral assemblages with the gross composition and texture of sandstones. *SEPM Journal of*
757 *Sedimentary Research*, Vol. *32*(3), 440–450. <https://doi.org/10.1306/74D70CE5-2B21-11D7-8648000102C1865D>
- 759 Janots, E., Engi, M., Rubatto, D., Berger, A., Gregory, C., & Rahn, M. (2009). Metamorphic rates in collisional
760 orogeny from in situ allanite and monazite dating. *Geology*, *37*(1), 11–14.
761 <https://doi.org/10.1130/G25192A.1>
- 762 Jochum, K. P., Stoll, B., Herwig, K., Willbold, M., Hofmann, A. W., Amini, M., & Aarburg, S. (2006). MPI-
763 DING reference glasses for in situ microanalysis: New reference values for element concentrations and
764 isotope ratios. *Geochemistry Geophysics Geosystems*, *7*. <https://doi.org/10.1029/2005GC001060>
- 765 Jollands, M. C., O’Neill, H. S. C., & Hermann, J. (2014). The importance of defining chemical potentials,
766 substitution mechanisms and solubility in trace element diffusion studies: the case of Zr and Hf in olivine.
767 *Contributions to Mineralogy and Petrology*, *168*(3), 1–19. <https://doi.org/10.1007/s00410-014-1055-x>
- 768 Kennan, P. S., & Murphy, F. C. (1993). Cotecule in lower Ordovician metasediments near the hidden Kentstown
769 granite, county Meath. *Irish Journal of Earth Sciences*, *12*, 41–46.

- 770 Kohn, M. J. (2009). Models of garnet differential geochronology. *Geochimica et Cosmochimica Acta*, 73(1),
 771 170–182. <https://doi.org/10.1016/j.gca.2008.10.004>
- 772 Kohn, M. J. (2014). “Thermoba-Raman-try”: Calibration of spectroscopic barometers and thermometers for
 773 mineral inclusions. *Earth and Planetary Science Letters*, 388, 187–196.
 774 <https://doi.org/10.1016/j.epsl.2013.11.054>
- 775 Kooijman, E., Mezger, K., & Berndt, J. (2010). Constraints on the U–Pb systematics of metamorphic rutile from
 776 in situ LA-ICP-MS analysis. *Earth and Planetary Science Letters*, 293(3–4), 321–330.
 777 <https://doi.org/10.1016/j.epsl.2010.02.047>
- 778 Ledent, D., Patterson, C., & Tilton, G. R. (1964). Ages of zircon and feldspar concentrates from North
 779 American beach and river sands. *The Journal of Geology*, 72(1), 112–122. <https://doi.org/10.1086/626967>
- 780 Liati, A., Gebauer, D., & Fanning, C. M. (2009). Geochronological evolution of HP metamorphic rocks of the
 781 Adula nappe, Central Alps, in pre-Alpine and Alpine subduction cycles. *Journal of the Geological
 782 Society*, 166, 797–810. <https://doi.org/10.1144/0016-76492008-033>. Geochronological
- 783 Ludwig, K. R. (2012). User’s manual for Isoplot 3.75: A geochronological toolkit for Microsoft Excel. *Berkeley
 784 Geochronology Center Special Publication*, 4, 70.
- 785 Machado, N., & Gauthier, G. (1996). Determination of ²⁰⁷Pb/²⁰⁶Pb ages on zircon and monazite by laser-
 786 ablation ICPMS and application to a study of sedimentary provenance and metamorphism in southeastern
 787 Brazil. *Geochimica et Cosmochimica Acta*, 60(24), 5063–5073. [https://doi.org/10.1016/S0016-
 788 7037\(96\)00287-6](https://doi.org/10.1016/S0016-7037(96)00287-6)
- 789 Malinovsky, D., Stenberg, A., Rodushkin, I., Andren, H., Ingri, J., Öhlander, B., & Baxter, D. C. (2003).
 790 Performance of high resolution MC-ICP-MS for Fe isotope ratio measurements in sedimentary geological
 791 materials. *Journal of Analytical Atomic Spectrometry*, 18(7), 687–695. <https://doi.org/10.1039/b302312e>
- 792 Malusà, M. G., Wang, J., Garzanti, E., Liu, Z., Villa, I. M., & Wittmann, H. (2017). Trace-element and Nd-
 793 isotope systematics in detrital apatite of the Po river catchment : Implications for provenance
 794 discrimination and the lag-time approach to detrital thermochronology. *LITHOS*, 290–291, 48–59.
 795 <https://doi.org/10.1016/j.lithos.2017.08.006>
- 796 Maneiro, K. A., Baxter, E. F., Samson, S. D., Marschall, H. R., & Hietpas, J. (2019). Detrital garnet
 797 geochronology: Application in tributaries of the French broad river, southern Appalachian mountains,
 798 USA. *Geology*, 47(12), 1189–1192. <https://doi.org/10.1130/G46840.1>
- 799 Mange, M. A., & Otvos, E. G. (2005). Gulf coastal plain evolution in West Louisiana: Heavy mineral
 800 provenance and Pleistocene alluvial chronology. *Sedimentary Geology*, 182(1–4), 29–57.
 801 <https://doi.org/10.1016/j.sedgeo.2005.07.015>
- 802 Manzotti, P., & Ballèvre, M. (2013). Multistage garnet in high-pressure metasediments: Alpine overgrowths on
 803 Variscan detrital grains. *Geology*, 41(11), 1151–1154. <https://doi.org/10.1130/G34741.1>
- 804 Mark, C., Cogné, N., & Chew, D. (2016). Tracking exhumation and drainage divide migration of the Western
 805 Alps: A test of the apatite U-Pb thermochronometer as a detrital provenance tool. *Bulletin of the
 806 Geological Society of America*, 128(9–10). <https://doi.org/10.1130/B31351.1>
- 807 Mark, C., Cogné, N., Chew, D., & Henrichs, I. (2018). Detecting orogenic wedge state and the rise of the
 808 External Alps by detrital thermochronology. *EarthArXiv* . <https://doi.org/10.31223/osf.io/d36xz>
- 809 Matte, P. (2001). The Variscan collage and orogeny (480–290 Ma) and the tectonic definition of the Armorica
 810 microplate: a review. *Terra Nova*, 13(2), 122–128. <https://doi.org/10.1046/j.1365-3121.2001.00327.x>
- 811 Mezger, K., Hanson, G. N., & Bohlen, S. R. (1989). U–Pb systematics of garnet: dating the growth of garnet in
 812 the late Archean Pikwitonei granulite domain at Cauchon and Natawahunan Lakes, Manitoba, Canada.
 813 *Contributions to Mineralogy and Petrology*, 101(2), 136–148. <https://doi.org/10.1007/BF00375301>
- 814 Milliken, K. L. (2007). Chapter 8 Provenance and Diagenesis of Heavy Minerals, Cenozoic Units of the
 815 Northwestern Gulf of Mexico Sedimentary Basin. *Developments in Sedimentology*.
 816 [https://doi.org/10.1016/S0070-4571\(07\)58008-8](https://doi.org/10.1016/S0070-4571(07)58008-8)
- 817 Millonig, L. J., Albert, R., Gerdes, A., Avigad, D., & Dietsch, C. (2020). Exploring laser ablation U–Pb dating
 818 of regional metamorphic garnet – The Straits Schist, Connecticut, USA. *Earth and Planetary Science
 819 Letters*, 552, 116589. <https://doi.org/10.1016/j.epsl.2020.116589>
- 820 Moecher, D., & Samson, S. D. (2006). Differential zircon fertility of source terranes and natural bias in the
 821 detrital zircon record: Implications for sedimentary provenance analysis. *Earth and Planetary Science
 822 Letters*, 247, 252–266. <https://doi.org/10.1016/j.epsl.2006.04.035>
- 823 Morton, A. C. (1985). A new approach to provenance studies: electron microprobe analysis of detrital garnets
 824 from Middle Jurassic sandstones of the northern North Sea. *Sedimentology*, 32(4), 553–566.
 825 <https://doi.org/10.1111/j.1365-3091.1985.tb00470.x>
- 826 Morton, A. C., & Hallsworth, C. (2007). Stability of Detrital Heavy Minerals During Burial Diagenesis. In M.
 827 Mange & D. Wright (Eds.), *Developments in Sedimentology* (Vol. 58, pp. 215–245). Elsevier.
 828 [https://doi.org/10.1016/S0070-4571\(07\)58007-6](https://doi.org/10.1016/S0070-4571(07)58007-6)

- 829 Najman, Y. (2006). The detrital record of orogenesis: A review of approaches and techniques used in the
 830 Himalayan sedimentary basins. *Earth-Science Reviews*, 74(1–2), 1–72.
 831 <https://doi.org/10.1016/j.earscirev.2005.04.004>
- 832 do Nascimento, D. R., Sawakuchi, A. O., Guedes, C. C. F., Giannini, P. C. F., Grohmann, C. H., & Ferreira, M.
 833 P. (2015). Provenance of sands from the confluence of the Amazon and Madeira rivers based on detrital
 834 heavy minerals and luminescence of quartz and feldspar. *Sedimentary Geology*, 316, 1–12.
 835 <https://doi.org/10.1016/j.sedgeo.2014.11.002>
- 836 Nicolaysen, L. O. (1961). Graphic interpretation of discordant age measurements on metamorphic rocks. *Annals*
 837 *of the New York Academy of Sciences*, 91(2), 198–206. [https://doi.org/10.1111/j.1749-](https://doi.org/10.1111/j.1749-6632.1961.tb35452.x)
 838 [6632.1961.tb35452.x](https://doi.org/10.1111/j.1749-6632.1961.tb35452.x)
- 839 Norris, A. & Danyushevsky, L. (2018). Towards Estimating the Complete Uncertainty Budget of Quantified
 840 Results Measured By LA-ICP-MS. *Goldschmidt*, Boston, USA
- 841 Oliver, G. J. H., Chen, F., Buchwaldt, R., & Hegner, E. (2000). Fast tectonometamorphism and exhumation in
 842 the type area of the Barrovian and Buchan zones. *Geology*, 28(5), 459. [https://doi.org/10.1130/0091-](https://doi.org/10.1130/0091-7613(2000)28<459:FTAET>2.0.CO;2)
 843 [7613\(2000\)28<459:FTAET>2.0.CO;2](https://doi.org/10.1130/0091-7613(2000)28<459:FTAET>2.0.CO;2)
- 844 O’Sullivan, G. J., Hoare, B. C., Mark, C., Drakou, F., & Tomlinson, E. L. (2023). Uranium–lead geochronology
 845 applied to pyrope garnet with very low concentrations of uranium. *Geological Magazine*, 1–10.
 846 <https://doi.org/10.1017/S0016756823000122>
- 847 Paton, C., Hellstrom, J., Paul, B., Woodhead, J., & Hergt, J. (2011). Iolite: Freeware for the visualisation and
 848 processing of mass spectrometric data. *Journal of Analytical Atomic Spectrometry*, 26, 2508.
 849 <https://doi.org/10.1039/c1ja10172b>
- 850 Raimondo, T., Payne, J., Wade, B., Lanari, P., Clark, C., & Hand, M. (2017). Trace element mapping by LA-
 851 ICP-MS : assessing geochemical mobility in garnet. *Contributions to Mineralogy and Petrology*, 172(4),
 852 1–22. <https://doi.org/10.1007/s00410-017-1339-z>
- 853 Rak, Z., Ewing, R., & Becker, U. (2011). Role of iron in the incorporation of uranium in ferric garnet matrices.
 854 *Physical Review B*, 84, 155128-1-155128–10. <https://doi.org/10.1103/PhysRevB.84.155128>
- 855 von Raumer, J. F., Bussy, F., & Stampfli, G. M. (2009). The Variscan evolution in the External massifs of the
 856 Alps and place in their Variscan framework. *Comptes Rendus - Geoscience*, 341(2–3), 239–252.
 857 <https://doi.org/10.1016/j.crte.2008.11.007>
- 858 Romer, R., & Smeds, S-A., (1996). U-Pb columbite ages of pegmatites from Sveconorwegian terranes in
 859 southwestern Sweden. *Precambrian Research*, 76, 15-30. [https://doi.org/10.1016/0301-9268\(95\)00023-2](https://doi.org/10.1016/0301-9268(95)00023-2)
- 860 Rubatto, D., & Hermann, J. (2003). Zircon formation during fluid circulation in eclogites (Monviso, Western
 861 Alps): implications for Zr and Hf budget in subduction zones. *Geochimica et Cosmochimica Acta*, 67(12),
 862 2173–2187. [https://doi.org/10.1016/S0016-7037\(02\)01321-2](https://doi.org/10.1016/S0016-7037(02)01321-2)
- 863 Salnikova, E., Stifeeva, M. V., Nikiforov, A. V., Yarmolyuk, A. V. V., & Kotov, A. B. (2018). Andradite –
 864 morimotoite garnets as promising U – Pb geochronometers for dating ultrabasic alkaline rocks. *Doklady*
 865 *Earth Sciences*, 480(5), 778–782. <https://doi.org/10.1134/S1028334X18060168>
- 866 Salnikova, E., Chakhmouradian, A. R., Stifeeva, M. V., Reguir, E. P., Kotov, A. B., Gritsenko, Y. D., &
 867 Nikiforov, A. V. (2019). Calcic garnets as a geochronological and petrogenetic tool applicable to a wide
 868 variety of rocks. *LITHOS*, 338–339, 141–154. <https://doi.org/10.1016/j.lithos.2019.03.032>
- 869 Schlunegger, F., Burbank, D. W., Matter, A., Engesser, B., & Mödden, C. (1996). Magnetostratigraphic
 870 calibration of the Oligocene to Middle Miocene (30–15 Ma) mammal biozones and depositional
 871 sequences of the Swiss Molasse Basin. *Eclogae Geologicae Helveticae*, 89, 753–788.
- 872 Schmid, S. M., Bernoulli, D., Fügenschuh, B., Matenco, L., Schefer, S., Schuster, R., et al. (2008). The Alpine-
 873 Carpathian-Dinaridic orogenic system: Correlation and evolution of tectonic units. *Swiss Journal of*
 874 *Geosciences*, 101(1), 139–183. <https://doi.org/10.1007/s00015-008-1247-3>
- 875 Schönig, J., von Eynatten, H., Tolosana-Delgado, R., & Meinhold, G. (2021). Garnet major-element
 876 composition as an indicator of host-rock type: a machine learning approach using the random forest
 877 classifier. *Contributions to Mineralogy and Petrology*, 176(12). [https://doi.org/10.1007/s00410-021-](https://doi.org/10.1007/s00410-021-01854-w)
 878 [01854-w](https://doi.org/10.1007/s00410-021-01854-w)
- 879 Schulz, B., & von Raumer, J. F. (2011). Discovery of Ordovician-Silurian metamorphic monazite in garnet
 880 metapelites of the Alpine External Aiguilles Rouges Massif. *Swiss Journal of Geosciences*, 104(1), 67–79.
 881 <https://doi.org/10.1007/s00015-010-0048-7>
- 882 Schuster, R., & Stüwe, K. (2008). Permian metamorphic event in the Alps. *Geology*, 36(8), 603–606.
 883 <https://doi.org/10.1130/G24703A.1>
- 884 Seman, S., Stockli, D. F., & Mclean, N. M. (2017). U-Pb geochronology of grossular-andradite garnet.
 885 *Chemical Geology*, 460(April), 106–116. <https://doi.org/10.1016/j.chemgeo.2017.04.020>
- 886 Simpson, A., Gilbert, S., Tamblyn, R., Hand, M., Spandler, C., Gillespie, J., et al. (2021). In-situ Lu–Hf
 887 geochronology of garnet, apatite and xenotime by LA ICP MS/MS. *Chemical Geology*, 577.
 888 <https://doi.org/10.1016/j.chemgeo.2021.120299>

- 889 Simpson, A., Glorie, S., Hand, M., Spandler, C., Gilbert, S., & Cave, B. (2022). In situ Lu-Hf geochronology of
 890 calcite. *Geochronology*, 4(1), 353–372. <https://doi.org/10.5194/gchron-4-353-2022>
- 891 Simpson, A., Glorie, S., Hand, M., Spandler, C., Gilbert, S. (2023). Garnet Lu-Hf speed dating: a novel method
 892 to rapidly resolve polymetamorphic histories. *Gondwana Research*.
- 893 Smith, M. P., Henderson, P., Jeffries, T. E. R., Long, J., & Williams, C. T. (2004). The rare earth elements and
 894 uranium in garnets from the Beinn an Dubhaich aureole, Skye, Scotland, UK: Constraints on processes in
 895 a dynamic hydrothermal system, *Journal of Petrology*, 45(3), 457–484.
 896 <https://doi.org/10.1093/petrology/egg087>
- 897 Smit, M. A., Scherer, E. E., & Mezger, K. (2013). Lu-Hf and Sm-Nd garnet geochronology: Chronometric
 898 closure and implications for dating petrological processes. *Earth and Planetary Science Letters*, 381, 222–
 899 233. <https://doi.org/10.1016/j.epsl.2013.08.046>
- 900 Stacey, J. S., & Kramers, J. D. (1975). Approximation of terrestrial lead isotope evolution by a two-stage model.
 901 *Earth and Planetary Science Letters*, 26, 207–221. [https://doi.org/10.1016/0012-821X\(75\)90088-6](https://doi.org/10.1016/0012-821X(75)90088-6)
- 902 Stampfli, G. M., & Hochard, C. (2009). Plate tectonics of the Alpine realm. *Geological Society, London, Special
 903 Publications*, 327(1), 89–111. <https://doi.org/10.1144/SP327.6>
- 904 Stifeeva, M. V., Salnikova, E. B., Samsonov, A. V., Kotov, A. B., & Gritsenko, Y. D. (2019). Garnet U–Pb Age
 905 of Skarns from Dashkesan Deposit (Lesser Caucasus). *Doklady Earth Sciences*, 487(2), 953–956.
 906 <https://doi.org/10.1134/S1028334X19080178>
- 907 Stutenbecker, L., Berger, A., & Schlunegger, F. (2017). The potential of detrital garnet as a provenance proxy in
 908 the Central Swiss Alps. *Sedimentary Geology*, 351, 11–20. <https://doi.org/10.1016/j.sedgeo.2017.02.002>
- 909 Stutenbecker, L., Tollan, P.M.E., Madella, A. & Lanari, P. (2019). Miocene basement exhumation in the Central
 910 Alps recorded by detrital garnet geochemistry in foreland basin deposits. *Solid Earth*, 10, 1581–1595.
 911 <https://doi.org/10.5194/se-10-1581-2019>
- 912 Suggate, S. M., & Hall, R. (2014). Using detrital garnet compositions to determine provenance: A new
 913 compositional database and procedure. *Geological Society Special Publication*, 386(1), 373–393.
 914 <https://doi.org/10.1144/SP386.8>
- 915 Thöni, M. (2003). Sm–Nd isotope systematics in garnet from different lithologies (Eastern Alps): age results,
 916 and an evaluation of potential problems for garnet Sm–Nd chronometry. *Chemical Geology*, 194(4), 353–
 917 379. [https://doi.org/10.1016/S0009-2541\(02\)00419-9](https://doi.org/10.1016/S0009-2541(02)00419-9)
- 918 Todd, C. S., & Engi, M. (1997). Metamorphic field gradients in the Central Alps. *Journal of Metamorphic
 919 Geology*, 15(4), 513–530. <https://doi.org/10.1111/j.1525-1314.1997.00038.x>
- 920 Velbel, M.A. (1984). Natural weathering mechanisms of almandine garnet. *Geology*, 12, 631–634.
 921 [https://doi.org/10.1130/0091-7613\(1984\)12<631:NWMOAG>2.0.CO;2](https://doi.org/10.1130/0091-7613(1984)12<631:NWMOAG>2.0.CO;2)
- 922 Vermeesch, P. (2012). On the visualisation of detrital age distributions. *Chemical Geology*, 312–313, 190–194.
 923 <https://doi.org/10.1016/j.chemgeo.2012.04.021>
- 924 Vermeesch, P. (2018). IsoplotR: A free and open toolbox for geochronology. *Geoscience Frontiers*, 9(5), 1479–
 925 1493. <https://doi.org/10.1016/j.gsf.2018.04.001>
- 926 Vervoort, J. D., Patchett, P. J., Blichert-Toft, J., & Albarède, F. (1999). Relationships between Lu-Hf and Sm-
 927 Nd isotopic systems in the global sedimentary system. *Earth and Planetary Science Letters* (Vol. 168).
- 928 Van Westrenen, W., Blundy, J., & Wood, B. (1999). Crystal-chemical controls on trace element partitioning
 929 between garnet and anhydrous silicate melt. *American Mineralogist*, 84, 838–847. Retrieved from
 930 <https://www.degruyter.com/document/doi/10.2138/am-1999-5-618/html>
- 931 Walker, S., Bird, A. F., Thirlwall, M. F., & Strachan, R. A. (2021). Caledonian and Pre-Caledonian orogenic
 932 events in Shetland, Scotland: evidence from garnet Lu–Hf and Sm–Nd geochronology. *Geological
 933 Society, London, Special Publications*, 503(1), 305–331. <https://doi.org/10.1144/SP503-2020-32>
- 934 White, R. W., Powell, R., & Johnson, T. E. (2014). The effect of Mn on mineral stability in metapelites
 935 revisited: New A-X relations for manganese-bearing minerals. *Journal of Metamorphic Geology*, 32(8),
 936 809–828. <https://doi.org/10.1111/jmg.12095>
- 937 Woods, G. (2016). Resolution of ^{176}Yb and ^{176}Lu interferences on ^{176}Hf to enable accurate $^{176}\text{Hf}/^{177}\text{Hf}$ isotope
 938 ratio analysis using an Agilent 8800 ICP-QQQ with MS/MS. Technical Note, Agilent Technologies, Inc.
 939 <https://doi.org/10.13140/RG.2.1.3971.6245>
- 940 Yakymchuk, C., Clark, C., & White, R. W. (2018). Phase Relations, Reaction Sequences and Petrochronology.
 941 *Reviews in Mineralogy and Geochemistry*, 83(1), 13–53. <https://doi.org/10.2138/rmg.2017.83.2>
- 942 Yang, Y. H., Wu, F. Y., Yang, J. H., Mitchell, R. H., Zhao, Z. F., Xie, L. W., et al. (2018). U-Pb age
 943 determination of schorlomite garnet by laser ablation inductively coupled plasma mass spectrometry.
 944 *Journal of Analytical Atomic Spectrometry*, 33(2), 231–239. <https://doi.org/10.1039/c7ja00315c>
- 945 Zack, T., Stockli, D. F., Luvizotto, G. L., Barth, M. G., Belousova, E., Wolfe, M. R., & Hinton, R. W. (2011). In
 946 situ U-Pb rutile dating by LA-ICP-MS: ^{208}Pb correction and prospects for geological applications.
 947 *Contributions to Mineralogy and Petrology*, 162(3), 515–530. <https://doi.org/10.1007/s00410-011-0609-4>

- 948 Zhao, Z. F., & Zheng, Y. F. (2007). Diffusion compensation for argon, hydrogen, lead, and strontium in
949 minerals: Empirical relationships to crystal chemistry. In *American Mineralogist* (Vol. 92, pp. 289–308).
950 Mineralogical Society of America. <https://doi.org/10.2138/am.2007.2127>
951 Zimmermann, S., Mark, C., Chew, D., & Voice, P. J. (2018). Maximising data and precision from detrital zircon
952 U-Pb analysis by LA-ICPMS: The use of core-rim ages and the single-analysis concordia age.
953 *Sedimentary Geology*. <https://doi.org/10.1016/j.sedgeo.2017.12.020>
954